

# Contrastive inverse regression for dimension reduction

Sam Hawke<sup>1</sup>, Hengrui Luo<sup>2</sup> and Didong Li<sup>1</sup>

*Department of Biostatistics, University of North Carolina at Chapel Hill<sup>1</sup>*

*Computational Research Division, Lawrence Berkeley Laboratory<sup>2</sup>*

## Abstract

Supervised dimension reduction (SDR) has been a topic of growing interest in data science, as it enables the reduction of high-dimensional covariates while preserving the functional relation with certain response variables of interest. However, existing SDR methods are not suitable for analyzing datasets collected from case-control studies. In this setting, the goal is to learn and exploit the low-dimensional structure unique to or enriched by the case group, also known as the foreground group. While some unsupervised techniques such as the contrastive latent variable model and its variants have been developed for this purpose, they fail to preserve the functional relationship between the dimension-reduced covariates and the response variable. In this paper, we propose a supervised dimension reduction method called contrastive inverse regression (CIR) specifically designed for the contrastive setting. CIR introduces an optimization problem defined on the Stiefel manifold with a non-standard loss function. We prove the convergence of CIR to a local optimum using a gradient descent-based algorithm, and our numerical study empirically demonstrates the improved performance over competing methods for high-dimensional data.

## 1 Introduction

Vogelstein et al. (2021) have highlighted the increasing importance of supervised dimension reduction (SDR) methodologies compared to unsupervised counterparts (e.g., principal component analysis (PCA), spherelets (Li et al., 2022), spherical rotation component analysis (Luo and Li, 2022), etc.) in data science. With the advent of large biological datasets, such as single-cell RNA sequencing data, dimension reduction (DR) has become a crucial step in the preprocessing of data for visualization, structural discovery, and downstream biological analyses.

Given paired observations  $(x, y) \in \mathbb{R}^p \times \mathbb{R}$ , where  $x$  consists of  $p$  covariates, and  $y$  is the corresponding response or output variable, the common assumption in SDR is that

$$y = \varphi(V^\top x, \epsilon), \text{ for some function } \varphi, \quad (1)$$

where  $V \in \mathbb{R}^{p \times d}$  with  $d \ll p$  is the projection matrix from a high-dimensional to a low-dimensional space,  $\epsilon$  is the measurement error independent of  $x$ , and  $\varphi$  is an arbitrary unknown function. For example, in a single-cell RNA sequencing dataset,  $x$  could be the expression of genes for a cell and  $y$  could be the cell type.

Under assumption (1), although the low-dimensional representation  $V^\top x$  is determined by a linear transformation, the function  $\varphi$  is an arbitrary unknown function. In this paper,

we stick to the assumption in (1) to focus on linear DR methods for two reasons. First, linear methods are computationally more efficient, particularly for large  $p$  and large  $n$ . Secondly, linear methods are more interpretable, which is an essential characteristic in scientific applications. For instance, in the example above, each column of  $V^\top x$  is often considered as a genetic pathway Bader et al. (2006). Although our proposed method can be extended to nonlinear cases by kernel method, we will leave this as future work.

Slice Inverse Regression (SIR, Li (1991)) is a well-established technique for supervised dimension reduction that is widely applicable in multiple scenarios due to its roots in regression analysis. It has been shown to have strong consistency results in both fixed dimensional (Hsing and Carroll, 1992) and high-dimensional (Lin et al., 2018) settings. The goal of SIR is to capture the most relevant low-dimensional linear subspace without any parametric or nonparametric model-fitting process for  $\varphi$ .

Moreover, SIR offers a geometric interpretation by conditioning on the sufficient statistics of the input distribution (Li, 1991; Cook and Weisberg, 1991). SIR incorporates the idea of linear dimension reduction with statistical sufficiency. In SIR, given a pair of features  $x \in \mathbb{R}^p$  and univariate response  $y \in \mathbb{R}$ , the goal is to find a matrix  $V \in \mathbb{R}^{p \times d}$ ,  $d < p$  such that  $y$  is conditionally independent of  $x$  given  $V^\top x$ . Although the matrix  $V$  is not identifiable, the column space of  $V$ , denoted  $\mathcal{C}(V)$ , is identifiable.

Motivated by emerging modern high-dimensional (Girard et al., 2022; Liao et al., 2023; Wilkinson and Luo, 2022) and biological datasets (Hilafu and Safo, 2022; Li and Yin, 2008), SIR evolved and admitted several generalizations, including localized SIR (Wu et al., 2008), kernel SIR (Wu et al., 2013), SIR with regularization (Li and Yin, 2008), SIR for longitudinal data (Jiang et al., 2014; Li et al., 2007), metric response values (Virta et al., 2022), and online SIR (Cai et al., 2020).

In this article, we focus on a specific type of high-dimensional biological data, where the dataset consists of two groups — a foreground group, also known as treatment group or case group, and a background group, also known as control group. The goal is to identify low-dimensional structure, variation, and information unique to the foreground group for downstream analysis. This situation arises naturally in many scientific experiments with two subpopulations. For example, in Electronic Health Record (EHR) data, the foreground data could be health-related covariates from patients who received certain medical treatment, while the background data could be measurements from healthy patients who did not receive any treatment. In this case, the goal is to identify a unique structure in patients who received the treatment that can predict future outcomes. In a genomics context, the foreground data could be gene expression measurements from patients with a disease, and the background data could be measurements from healthy people. In this case, the goal is to predict a certain phenotype for the diseased patient for disease analysis and future therapy.

Previous contrastive models, such as the contrastive latent variable model (CLVM, Zou et al. (2013)), contrastive principal component analysis (CPCA, Abid et al. (2018)), probabilistic contrastive principal component analysis (PCPCA, Li et al. (2020)), and the contrastive Poisson latent variable model (CPLVM, Jones et al. (2022)), have shown that using

the case-control structure between foreground and background groups can greatly improve the effectiveness of dimension reduction over standard DR methods such as PCA and its variants. However, to the best of our knowledge, none of these unsupervised contrastive dimension reduction methods is directly applicable to SDR setting.

In this work, we move from these unsupervised contrastive dimension reduction methods to a supervised contrastive dimension reduction setting. By combining the idea of contrastive loss function and the sufficient dimension reduction considered in the SIR model, we propose the Contrastive Inverse Regression (CIR) model, which exactly recovers SIR when a certain parameter is zero. The CIR model sheds light on how to explore and exploit the contrastive structures in supervised dimension reduction.

Table 1: Categorization of DR methods by whether they are supervised or contrastive.

		Supervised	
		No	Yes
Contrastive	No	PCA, CCA	SIR, LDA, LASSO
	Yes	CPCA, PCPCA	<b>CIR</b>

Table 1 lists several popular DR methods and their properties. The table categorizes these methods as “contrastive” and “supervised”, based on whether they are designed for case-control data and able to identify low-dimensional structure unique to the case group, and if they take the response variable  $y$  into consideration and use  $V^\top x$  to predict  $y$ . For example, PCA, the most well known DR method, is neither contrastive nor supervised. Similarly, canonical correlation analysis (CCA, Hotelling (1992)) does not utilize  $y$  or the unique information of one group, which makes it neither contrastive nor supervised. Methods such as CLVM, CPCA, PCPCA, and CPLVM are contrastive but not supervised. On the other hand, classical supervised DR methods including SIR (Li, 1991), linear discriminant analysis (LDA, Hastie et al. (1994)), and the least absolute shrinkage and selection operator (LASSO, Tibshirani (1996)) are supervised but not contrastive. Our proposed method, CIR, combines both contrastive and supervised features by utilizing both response  $y$  and the case-control structure.

It is important to note that the assumption (1) does not limit the response variable  $y$  to be continuous or categorical, and thus we do not distinguish between regression and classification. However, some methods listed in Table 1 are specifically designed for either continuous  $y$  (regression, LASSO) or categorical  $y$  (classification, LDA). CIR handles both scenarios with the only difference being in the choice of slices, as explained in Section 2. Furthermore, not all existing DR methods are included in this table. For example, the recently proposed linear optimal low-rank projection (LOL, Vogelstein et al. (2021)) is designed for the classification setting and requires the number of classes to be smaller than the reduced dimension  $d$ . This can be restrictive, for example, when applied to a single-cell RNA sequencing dataset, where  $d$  is required to be greater than number of cell types. In

contrast, CIR does not require such data-dependent constraints on the reduced dimension  $d$ . Similarly, data visualization algorithms that require  $d = 2$  such as the t-distributed stochastic neighbor embedding (tSNE, Van der Maaten and Hinton (2008)) and uniform manifold approximation and projection (UMAP, Becht et al. (2019)) are not listed in the table.

We now present our proposed methodology, including an algorithm for solving the associated nonconvex optimization problem on the Stiefel manifold. We also provide analysis of the convergence of the algorithm, and conduct extensive experiments to demonstrate its superior performance on high-dimensional biomedical datasets when compared to existing DR methods. All proofs and additional experimental details are provided in the appendix.

## 2 Method

To maintain consistency, we will use the terms “foreground group” and “background group” instead of “case-control” or “treatment-control” in the remaining sections. We first briefly review SIR as our motivation.

**Definition 1.** (*Stiefel manifold*)  $\text{St}(p, d) := \{V \in \mathbb{R}^{p \times d} : V^\top V = I_d\}$  admits a smooth manifold structure equipped with a Riemannian metric, called the *Stiefel manifold*.

Recall that under the assumption in Equation (1), the centered inverse regression curve,  $\mathbb{E}[x|y] - \mathbb{E}[x]$ , lies exactly in the linear space spanned by columns of  $\Sigma_{xx}V$ , denoted by  $\mathcal{C}(\Sigma_{xx}V)$ , where  $\Sigma_{xx}$  is the covariance matrix of  $x$ . This linear subspace is called the *effective dimension reduced* (e.d.r.) space (Li, 1991). As a result, the objective of SIR is to minimize the expected squared distance between  $\mathbb{E}[x|y]$  and  $\mathcal{C}(\Sigma_{xx}V)$ :

$$\min_{V \in \text{St}(p, d)} \mathbb{E}_y [d^2(\mathbb{E}[x|y] - \mathbb{E}[x], \mathcal{C}(\Sigma_{xx}V))] \quad (2)$$

where  $d$  is the Euclidean distance.

In the contrastive setting, denote foreground data by  $(x, y) \in \mathbb{R}^p \times \mathbb{R}$  and background data by  $(\tilde{x}, \tilde{y}) \in \mathbb{R}^p \times \mathbb{R}$ . For convenience, we assume that  $x$  and  $\tilde{x}$  are centered at the origin so that  $\mathbb{E}[x] = \mathbb{E}[\tilde{x}] = 0$ . Our goal is to find a low-dimensional representation of  $x$ , denoted by  $V^\top x$ , such that  $y$  is determined by  $V^\top x$  while  $\tilde{y}$  is not determined by  $V^\top \tilde{x}$ . The goal of CIR is to find a low-dimensional subspace represented by  $V$  such that

$$\begin{cases} y = \varphi(V^\top x, \epsilon) \\ \tilde{y} \neq \varphi(V^\top \tilde{x}, \tilde{\epsilon}) \end{cases} \quad (3)$$

for some unknown function  $\varphi$ . That is, the column space of  $V$  captures the low-dimensional information unique to the foreground group so that we can use  $V^\top x$  to predict  $y$ . Instead of optimizing a single loss similar to SIR, CIR aims at optimizing the subspace  $\mathcal{C}(\Sigma_{xx}V)$  to minimize the “contrastive loss function”:

$$f(V) := \mathbb{E}_y [d^2(\mathbb{E}[x | y], \mathcal{C}(\Sigma_{xx}V))] - \alpha \mathbb{E}_{\tilde{y}} [d^2(\mathbb{E}[\tilde{x} | \tilde{y}], \mathcal{C}(\Sigma_{\tilde{x}\tilde{x}}V))], \quad (4)$$

where  $\alpha \geq 0$ ,  $\Sigma_{xx} = \text{Cov}(X)$  and  $\Sigma_{\tilde{x}\tilde{x}} = \text{Cov}(\tilde{X}) \in \mathbb{R}^{p \times p}$ , and  $d$  is the Euclidean distance. Define the following notation:

$$\begin{aligned} v_y &= \mathbb{E}[x | y], \quad v_{\tilde{y}} = \mathbb{E}[\tilde{x} | \tilde{y}] \in \mathbb{R}^p \\ \Sigma_x &= \text{Cov}(v_y), \quad \Sigma_{\tilde{x}} = \text{Cov}(v_{\tilde{y}}) \in \mathbb{R}^{p \times p} \end{aligned}$$

$v_y$  (and  $v_{\tilde{y}}$ ) are called the centered inverse regression curve (Li, 1991; Virta et al., 2022). The resulting loss function  $f$  balances the effectiveness of dimension reduction between the foreground and background groups. We can adjust the hyperparameter  $\alpha$  to express our belief in the importance of the background group. Note that the parameter  $\alpha$  appears naturally in other contrastive DR methods, including CPCA and PCPCA.

We need to simplify the loss function  $f(V)$  for subsequent analyses. Recall that the projection to the subspace  $\mathcal{C}(\Sigma_{xx}V)$  and  $\mathcal{C}(\Sigma_{\tilde{x}\tilde{x}}V)$  is given by the following projection matrices:

$$\begin{aligned} P_{\Sigma_{xx}V} &:= \Sigma_{xx}V \left[ V^\top \Sigma_{xx}^2 V \right]^{-1} V^\top \Sigma_{xx} \\ P_{\Sigma_{\tilde{x}\tilde{x}}V} &:= \Sigma_{\tilde{x}\tilde{x}}V \left[ V^\top \Sigma_{\tilde{x}\tilde{x}}^2 V \right]^{-1} V^\top \Sigma_{\tilde{x}\tilde{x}}. \end{aligned}$$

Because projection matrices are idempotent, that is,  $P_{\Sigma_{xx}V}^2 = P_{\Sigma_{xx}V}$  and  $P_{\Sigma_{\tilde{x}\tilde{x}}V}^2 = P_{\Sigma_{\tilde{x}\tilde{x}}V}$ , we can rewrite the loss function as follows:

$$\begin{aligned} f(V) &= \mathbb{E}_y \left[ d^2(\mathbb{E}[x | y], \mathcal{C}(\Sigma_{xx}V)) \right] - \alpha \mathbb{E}_{\tilde{y}} \left[ d^2(\mathbb{E}[\tilde{x} | \tilde{y}], \mathcal{C}(\Sigma_{\tilde{x}\tilde{x}}V)) \right] \\ &= \mathbb{E}_y \left[ \|v_y - P_{\Sigma_{xx}V} v_y\|^2 \right] - \alpha \mathbb{E}_{\tilde{y}} \left[ \|v_{\tilde{y}} - P_{\Sigma_{\tilde{x}\tilde{x}}V} v_{\tilde{y}}\|^2 \right] \\ &= \mathbb{E}_y \left[ v_y^\top v_y - v_y^\top P_{\Sigma_{xx}V} v_y \right] - \alpha \mathbb{E}_{\tilde{y}} \left[ v_{\tilde{y}}^\top v_{\tilde{y}} - v_{\tilde{y}}^\top P_{\Sigma_{\tilde{x}\tilde{x}}V} v_{\tilde{y}} \right] \\ &= \mathbb{E}_y \left[ v_y^\top v_y - v_y^\top P_{\Sigma_{xx}V} v_y \right] - \alpha \mathbb{E}_{\tilde{y}} \left[ v_{\tilde{y}}^\top v_{\tilde{y}} - v_{\tilde{y}}^\top P_{\Sigma_{\tilde{x}\tilde{x}}V} v_{\tilde{y}} \right] \end{aligned}$$

The solution to the optimization problem defined by this loss function, if it exists, leads to our CIR model.

We remove the constant terms  $\mathbb{E}_y[v_y^\top v_y]$  and  $\mathbb{E}_{\tilde{y}}[v_{\tilde{y}}^\top v_{\tilde{y}}]$  that are independent of  $V$  and continue to simplify  $f(V)$ :

$$\begin{aligned} f(V) &= -\mathbb{E}_y[v_y^\top P_{\Sigma_{xx}V} v_y] + \alpha \mathbb{E}_{\tilde{y}}[v_{\tilde{y}}^\top P_{\Sigma_{\tilde{x}\tilde{x}}V} v_{\tilde{y}}] \\ &= -\mathbb{E}_y[\text{tr}(v_y^\top P_{\Sigma_{xx}V} v_y)] + \alpha \mathbb{E}_{\tilde{y}}[\text{tr}(v_{\tilde{y}}^\top P_{\Sigma_{\tilde{x}\tilde{x}}V} v_{\tilde{y}})] \\ &= -\text{tr}(\Sigma_x P_{\Sigma_{xx}V}) + \alpha \text{tr}(\Sigma_{\tilde{x}} P_{\Sigma_{\tilde{x}\tilde{x}}V}) \\ &= -\text{tr} \left( V^\top \Sigma_{xx} \Sigma_x \Sigma_{xx} V \left[ V^\top \Sigma_{xx}^2 V \right]^{-1} \right) + \alpha \text{tr} \left( V^\top \Sigma_{\tilde{x}\tilde{x}} \Sigma_{\tilde{x}} \Sigma_{\tilde{x}\tilde{x}} V \left[ V^\top \Sigma_{\tilde{x}\tilde{x}}^2 V \right]^{-1} \right) \\ &= -\text{tr}(V^\top A V (V^\top B V)^{-1}) + \alpha \text{tr}(V^\top \tilde{A} V (V^\top \tilde{B} V)^{-1}), \end{aligned}$$

where  $A = \Sigma_{xx}\Sigma_x\Sigma_{xx}$ ,  $B = \Sigma_{xx}^2$ ,  $\tilde{A} = \Sigma_{\tilde{x}\tilde{x}}\Sigma_{\tilde{x}}\Sigma_{\tilde{x}\tilde{x}}$ , and  $\tilde{B} = \Sigma_{\tilde{x}\tilde{x}}^2$ .

Thus, in the case where  $\alpha = 0$ , CIR reduces to SIR. In this case, the problem can be reparameterized by  $V^* = B^{1/2}V$  so that the columns are orthogonal, which reduces the loss function to a quadratic form, yielding a closed-form solution (a generalized eigenproblem). In the case where  $\alpha > 0$ , however, we cannot perform the same trick for both  $B$  and  $\tilde{B}$ , so we must resort to numerical approximations. We adopt gradient-based optimization algorithms on  $\text{St}(p, d)$ , which are based on the gradient of  $f$  given by the following lemma.

**Lemma 1.** *The gradient of  $f$  is given by*

$$-\frac{1}{2} \text{grad } f(V) = AV(V^\top BV)^{-1} - BV(V^\top BV)^{-1}V^\top AV(V^\top BV)^{-1} \\ - \alpha \left( \tilde{A}V(V^\top \tilde{B}V)^{-1} - \tilde{B}V(V^\top \tilde{B}V)^{-1}V^\top \tilde{A}V(V^\top \tilde{B}V)^{-1} \right).$$

Note that the gradient  $\text{grad } f$  is different from the standard gradient in Euclidean space, denoted by  $Df = \frac{\partial f}{\partial V}$ . The difference is that  $\text{grad } f$  lies in the tangent space of  $\text{St}(p, d)$  at  $V$ , while the Euclidean version may escape from the tangent space.

**Theorem 1.** *If  $V$  is a local minimizer of the optimization problem (4), then*

$$AVE(V) - \alpha \tilde{A}V\tilde{E}(V) = BVF(V) - \alpha \tilde{B}V\tilde{F}(V),$$

where  $E(V) = (V^\top BV)^{-1}$ ,  $\tilde{E}(V) = (V^\top \tilde{B}V)^{-1}$ ,  $F(V) = (V^\top BV)^{-1}V^\top AV(V^\top BV)^{-1}$ , and  $\tilde{F}(V) = (V^\top \tilde{B}V)^{-1}V^\top \tilde{A}V(V^\top \tilde{B}V)^{-1}$ .

Let  $G(V) = V^\top AV$  and  $\tilde{G}(V) = V^\top \tilde{A}V$ . Note, then, that the local optimality condition is equivalent to

$$AVE(V) - \alpha \tilde{A}V\tilde{E}(V) = BVE(V)G(V)E(V) - \alpha \tilde{B}V\tilde{E}(V)\tilde{G}(V)\tilde{E}(V). \quad (5)$$

In Appendix F, we discuss how Equation (5) may lead to a gradient-free algorithm that involves solving an asymmetric algebraic Riccati equation.

So far, we have discussed the population version, which relies on the distributions of  $x$ ,  $\tilde{x}$ ,  $y$ , and  $\tilde{y}$  that are unknown in practice. In real applications, we observe finite samples  $(x_i, y_i)_{i=1}^n$  as foreground data and  $(\tilde{x}_j, \tilde{y}_j)_{j=1}^m$  as background data. We denote  $X \in \mathbb{R}^{n \times p}$ ,  $\tilde{X} \in \mathbb{R}^{m \times p}$  where each row represents a sample; similarly, each entry of  $Y \in \mathbb{R}^n$  and  $\tilde{Y} \in \mathbb{R}^m$  represents a response value. In this case, we can replace the expectation by the sample mean to get estimates of  $\Sigma_x$ ,  $\Sigma_{\tilde{x}}$ ,  $\Sigma_{xx}$ , and  $\Sigma_{\tilde{x}\tilde{x}}$  and have the corresponding plug-in estimates for  $A$ ,  $B$ ,  $\tilde{A}$ , and  $\tilde{B}$ . Then, optimization reduces to a manifold optimization problem (Absil et al., 2009). The estimates of  $\Sigma_x$  and  $\Sigma_{\tilde{x}}$  deserve further discussion. As shown by Li (1991) and Cai et al. (2020) among others, for continuous response  $y$ , the observed support of response  $y$  can be discretized into *slices*  $I_h = (q_{h-1}, q_h]$ , for  $h = 1, \dots, H$ . An estimate of  $\Sigma_x$  is given by  $\sum_{h=1}^H m_h m_h^\top$  where  $m_h = \frac{1}{np_h} \sum_{y_i \in I_h} x_i$  with  $p_h = \frac{1}{n} \sum_{i=1}^n I(y_i \in I_h)$ . On the

---

**Algorithm 1:** CIR

---

**Input:** Foreground data  $(X, Y) \in \mathbb{R}^{n \times p} \times \mathbb{R}^n$ , Background data  $(\tilde{X}, \tilde{Y}) \in \mathbb{R}^{m \times p} \times \mathbb{R}^m$ ,  $\alpha > 0$ ,  $d \in \mathbb{Z}_+$ .

$$x_i = x_i - \frac{1}{n} \sum_{i=1}^n x_i; \tilde{x}_j = \tilde{x}_j - \frac{1}{m} \sum_{j=1}^m \tilde{x}_j$$

$$\Sigma_{xx} = \frac{1}{n} \sum_{i=1}^n x_i x_i^\top; \Sigma_{\tilde{x}\tilde{x}} = \frac{1}{m} \sum_{j=1}^m \tilde{x}_j \tilde{x}_j^\top.$$

**for**  $h = 1, \dots, H$  **do**

    Calculate slice proportions  $p_h = \frac{1}{n} \sum_{i=1}^n I(y_i \in I_h)$ .

    Calculate slice mean  $m_h = \frac{1}{np_h} \sum_{y_i \in I_h} x_i$ .

**end for**

$$\Sigma_x = \sum_{h=1}^H m_h m_h^\top.$$

**for**  $\tilde{h} = 1, \dots, \tilde{H}$  **do**

    Calculate slice proportions  $p_{\tilde{h}} = \frac{1}{m} \sum_{j=1}^m I(\tilde{y}_j \in I_{\tilde{h}})$ .

    Calculate slice mean  $m_{\tilde{h}} = \frac{1}{mp_{\tilde{h}}} \sum_{\tilde{y}_j \in I_{\tilde{h}}} \tilde{x}_j$ .

**end for**

$$\Sigma_{\tilde{x}} = \sum_{\tilde{h}=1}^{\tilde{H}} m_{\tilde{h}} m_{\tilde{h}}^\top.$$

Compute  $A = \Sigma_{xx} \Sigma_x \Sigma_{xx}$ ,  $B = \Sigma_{xx}^2$ ,  
 $\tilde{A} = \Sigma_{\tilde{x}\tilde{x}} \Sigma_{\tilde{x}} \Sigma_{\tilde{x}\tilde{x}}$ ,  $\tilde{B} = \Sigma_{\tilde{x}\tilde{x}}^2$ .

Find  $V^* = \arg \min_{V \in \text{St}(p,d)} f(V; A, B, \tilde{A}, \tilde{B}, \alpha)$  for  $f$  defined in (4).

**Return**  $V^*$ .

---

other hand, if  $y$  and  $\tilde{y}$  are categorical, the slices are naturally chosen as all possible values of  $y$  and  $\tilde{y}$ . Combining these pieces, we present our empirical version of the CIR algorithm in Algorithm 1.

It is worth noting that our optimization of  $f$  as a function of  $V \in \text{St}(p, d)$  cannot be considered as an optimization problem in  $\mathbb{R}^{p \times d}$  with orthogonality constraints  $V^\top V = I_d$  (Edelman et al., 1998; Boumal et al., 2019). Because the term  $(V^\top B V)^{-1}$  in  $f$  is not well defined unless  $V$  is full rank, our loss function  $f$  cannot be extended to the full Euclidean space  $\mathbb{R}^{p \times d}$ . We consider it as an optimization problem *intrinsically defined* on  $\text{St}(p, d)$  as laid out by Absil et al. (2009). This key property excludes some commonly used optimizers on manifolds, and we will discuss more details in the next section.

### 3 Theory

In this section, we discuss two concrete optimization algorithms for the last step in Algorithm 1 to find  $V^*$  and show their convergence. The optimization problem outlined in Equation (4) does not follow the classic Li-Duan theorem for regression-based dimension reduction (See

---

**Algorithm 2:** SGPM (Oviedo and Dalmau, 2019)

---

**Input:**  $V_0 \in \text{St}(p, d)$ ,  $\eta \in [0, 1]$ ,  $\mu, \rho_1, \epsilon, \delta \in (0, 1)$ .  
Set  $Q_0 = 1, C_0 = f(V_0)$ , and  $k = 0$   
**while**  $\|\nabla_V \mathcal{L}(V_k)\| > \epsilon$  **do**  
  Set  $A = \nabla f(V_k)V_k^\top - V_k \nabla f(V_k)^\top$   
  Set  $D_{\mu, \tau_k} = (I_p + \mu \tau_k A)^{-1}$   
  Let  $Y(\tau) := V_k - \tau(I_p - \mu \tau A)^{-1} \nabla f(V_k)$   
  Pick  $\tau_k > 0$  so that  $f(Y(\tau_k)) > C_k + \rho_1 \tau_k Df(X_k)[\dot{Y}(0)]$   
  Update  $V_{k+1} = \pi(V_k - \tau D_{\mu, \tau} \nabla f(V_k))$   
  Update  $\mu$  and  $C_{k+1}$   
  Set  $k = k + 1$   
**end while**  
 $V^* = V_k$

---

e.g., Cook (2009), Prop 8.1), due to its nonconvex nature. The convergence of the algorithm is discussed in detail below.

The first algorithm we consider is the scaled gradient projection method (SGPM) specifically designed for optimization on the Stiefel manifold (Oviedo and Dalmau, 2019). We first define an analog to Lagrangian multiplier  $\mathcal{L}(V, \Lambda) := f(V) - \frac{1}{2} \langle \Lambda, V^\top V - I_d \rangle$ , then the SGPM algorithm is summarized in Algorithm 2, where  $\pi(X) = \arg \min_{Q \in \text{St}(p, d)} \|X - Q\|_F$  is the orthogonal projection to the Stiefel manifold. Note for Algorithm 2 that the update for  $\mu$  and  $C_{k+1}$  is intricate; see Oviedo and Dalmau (2019) for more details.

To study the convergence of Algorithm 2, we need to study the Karush-Kuhn-Tucker (KKT) conditions for CIR:

**Definition 2** (Oviedo and Dalmau (2019)). *The KKT conditions are given by*

$$\begin{aligned} D_V \mathcal{L}(V, \Lambda) &= \nabla f - V \Lambda = 0 \\ D_\Lambda \mathcal{L}(V, \Lambda) &= V^\top V - I_d. \end{aligned}$$

Now we can state the convergence theorem of Algorithm 2:

**Theorem 2.** *Let  $\{V_k\}_{k=1}^\infty$  be an infinite sequence generated by Algorithm 2, then any accumulation point  $V_*$  of  $\{V_k\}_{k=1}^\infty$  satisfies the KKT conditions in Lemma 2, and  $\lim_{k \rightarrow \infty} \|D_V \mathcal{L}(V_k)\| = 0$ .*

Although Algorithm 2 is guaranteed to converge, there are two drawbacks. First, the accumulation point  $V_*$  is only guaranteed to satisfy the KKT conditions, but not necessarily be a critical point. Second, we do not know how fast  $V_k$  will converge to  $V_*$ . Next, we introduce an accelerated line search (ALS) algorithm as an alternative to SGPM that converges to a critical point with a known convergence rate. ALS is summarized by Algorithm 3, where



---

**Algorithm 3:** ALS (Absil et al., 2009)

---

**Input:**  $V_0 \in \text{St}(p, d)$ , retraction  $R$  from  $T\text{St}(p, d)$  to  $\text{St}(p, d)$ ; scalars  $\bar{\alpha} > 0$ ,  $c, \beta, \sigma \in (0, 1)$ .

**for**  $k = 0, 1, \dots$  **do**

$\eta_k = -\text{grad } f(V_k)$

Select  $V_{k+1}$  so that  $f(V_k) - f(V_{k+1}) \geq c(f(V_k) - f(R_{V_k}(t_k^A \eta_k)))$

**end for**

---

$t_k^A$  is the step size, called the Armijo step size for given  $\bar{\alpha}, \beta, \sigma, \eta_k$  and  $R$  is a retraction to  $\text{St}(p, d)$ , see Absil et al. (2009) for more details.

Algorithm 3 can be shown to have linear convergence to critical points if the hyperparameters are chosen properly. For other choices of  $\eta_k$ , see Appendix D for more details. The following adaptation of Theorem 4.5.6 in Absil et al. (2009) indicates linear convergence to stationary points.

**Theorem 3.** *Let  $\{V_k\}_{k=1}^\infty$  be an infinite sequence generated by Algorithm 3 with  $\eta_k = -\text{grad } f(V_k)$  converging to an accumulation point  $V_*$  of  $\{V_k\}_{k=1}^\infty$ , then  $V_*$  is a critical point of  $f$ , and  $\lim_{k \rightarrow \infty} \|\text{grad } f(V_k)\| = 0$ .*

*Furthermore, assuming  $V_*$  is a local minimizer of  $f$  with  $0 < \lambda_l := \min \text{eig}(\text{Hess}(f)(V_*))$  and  $\lambda_u := \max \text{eig}(\text{Hess}(f)(V_*))$ , then, for any  $r \in (r_*, 1)$  where*

$$r_* := 1 - \min \left( 2\sigma\bar{\alpha}\lambda_l, 4\sigma(1-\sigma)\beta\frac{\lambda_l}{\lambda_u} \right),$$

*there exists an integer  $K \neq 0$  such that*

$$f(V_{k+1}) - f(V_*) \leq (r + (1-r)(1-c))(f(V_k) - f(V_*)),$$

*for all  $k \geq K$ , where  $\bar{\alpha}, \beta, \sigma, c$  are the hyperparameters in Algorithm 3.*

The difference between Algorithm 2 and 3 deserves further comment. While we empirically observe that Algorithm 2 often converges faster, Algorithm 3 has theoretical properties which allow for a proof of linear convergence in terms of an upper bound on the number of iterations. In practice, for smaller datasets we suggest running Algorithm 3, while for larger datasets we recommend using Algorithm 2 for efficiency.

The computational complexity of CIR for both the SGPM-based optimization and the ALS-based optimization is compared to various competitors in the table below. Here, we assume that  $1 \leq d < p < m, n$ , where the background and foreground data have  $m$  and  $n$  samples, respectively. Specifically, we assume that  $\epsilon$  denotes the stopping error such that  $f(V_k) - f(V_*) \leq \epsilon$ . It is noteworthy that a  $p$ -dimensional singular value decomposition can be achieved within  $\mathcal{O}(p^3)$ . We present the comparison in the table below.

Table 2: Computational Time-Complexity of CIR and Competitors

Algorithm	Theoretical Algorithmic Complexity
CIR, SGPM-based	$\mathcal{O}((m+n)p^2)$
CIR, ALS-based	$\mathcal{O}(-\log(\epsilon)p^3 + (m+n)p^2)$
LDA	$\mathcal{O}(np^2)$
PCA	$\mathcal{O}(np^2)$
CPCA	$\mathcal{O}((m+n)p^2)$
SIR	$\mathcal{O}(np^2)$

## 4 Application

When applying CIR, several hyperparameters must be tuned, such as the weight  $\alpha$ , the reduced dimension  $d$ , and the slices  $I_h$  and  $I_{\tilde{h}}$  for estimation of  $\Sigma_x$  and  $\Sigma_{\tilde{x}}$ . In some cases, it may also be necessary to determine the definition of the foreground and background groups and to assign background labels  $\tilde{Y}$ .

The value of  $\alpha \geq 0$  can be determined by cross-validation. Our numerical experiments show that CIR is robust to the choice of  $\alpha$ ; that is, the performance of the method changes continuously with  $\alpha$ . Tables supporting this observation are provided in G.1 and G.2.

Additionally, the choice of reduced dimension  $d$  may depend on the goal of the investigator. If visualization is considered important,  $d = 2$  is appropriate. If the goal is prediction, the elbow point of the  $d$  versus prediction error plot may suggest an optimal  $d$ . However, as with other DR methods, determining the optimal value of  $d$  is still a topic of ongoing research Camastra and Staiano (2016); Campadelli et al. (2015).

The definition of foreground data  $X$  and  $Y$  should be the data and the target variable of interest, while the choices of background data  $\tilde{X}$  and  $\tilde{Y}$  may not be as straightforward. These data are intended to represent “noise” that is “subtracted” from the foreground data. For example, in the biomedical context, if the population of interest is a group of sick patients, the background dataset may include observations of healthy individuals. In other contexts, however, it may be appropriate to use  $\tilde{X} = X$ . In this case, the choice of background label  $\tilde{Y}$  may be unclear. If another outcome variable was collected, it could be used as  $\tilde{Y}$ ; otherwise, randomly selected values in the support of  $Y$  could be used to represent “noise”.

The estimates for  $\Sigma_x$  and  $\Sigma_{\tilde{x}}$  are partly determined by whether  $y$  and  $\tilde{y}$  are categorical or continuous. If these variables are categorical, then each value of  $y$  (or  $\tilde{y}$ ) can be considered as a separate slice, resulting in  $|\text{supp}(Y)|$  (or  $|\text{supp}(\tilde{Y})|$ ) total slices. On the other hand, if these variables are continuous, slices can be taken to represent an equally spaced partition of the range of  $Y$  (or  $\tilde{Y}$ ), with the number of slices being tunable hyperparameters.

## 4.1 Mouse Protein

The first dataset we considered was collected for the purpose of identifying proteins critical to learning in a mouse model of Down syndrome Higuera et al. (2015). The data contain 1095 observations of expression levels of 77 different proteins, along with genotype (t=Ts65Dn, c=control), behavior (CS=context-shock, SC=shock-context), and treatment (m=memantine, s=saline). The behavior of CS corresponds to the scenario in which the mouse was first placed in a new cage and permitted to explore for a few minutes before being exposed to a brief electric shock; conversely, SC corresponds to mice immediately given an electric shock upon being placed in a new cage, and then being permitted to explore. Of the data, 543 samples contain at least one missing value. Taking into account the relatively large sample size, we consider only the 552 observations with complete data. We do not perform any normalization or any other type of preprocessing to the raw data prior to analysis.

In this example,  $X \in \mathbb{R}^{552 \times 77}$  represents the expression of 77 proteins of all mice without a missing value, while  $y_i \in \{0, 1, \dots, 7\}$  represents the combination of 3 binary variables: genotype, treatment, and behavior. For example,  $y_i = 1$  means that the  $i$ -th mouse received memantine, was exposed to context-shock, and has genotype Ts65Dn. To visualize the data, we apply unsupervised DR algorithms PCA, tSNE and UMAP to  $X$  and supervised DR methods LDA, LASSO and SIR to  $(X, Y)$ , with  $d = 2$  for all algorithms. The 2-dimensional representation is given in Figure 1, where each color represents a class of mice among 8 total classes.

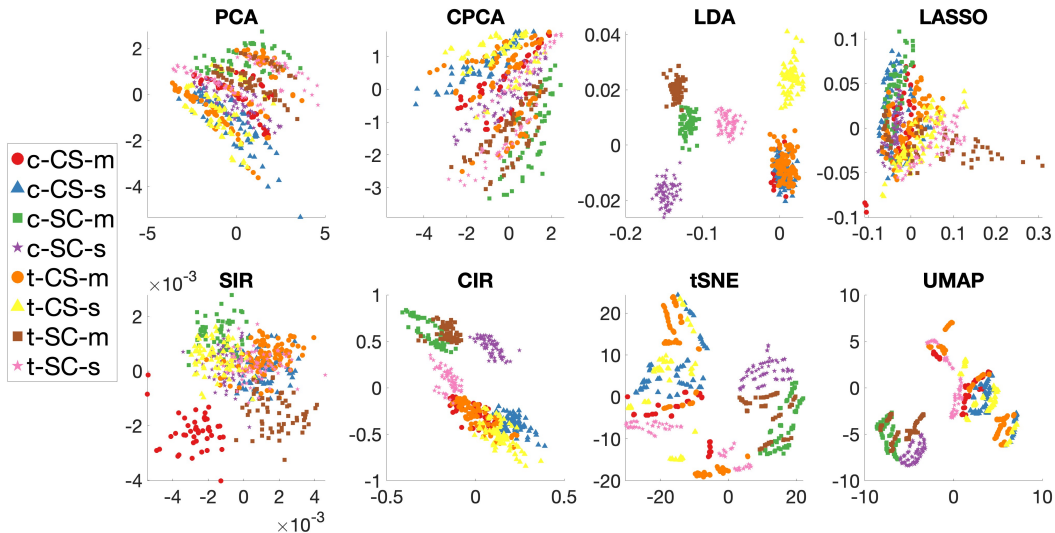


Figure 1: 2-d representation of mouse protein data

PCA, LASSO, SIR, tSNE, and UMAP fail to distinguish between classes, whereas LDA successfully separates 5 classes but with 3 classes (c-CS-m, t-CS-m, t-CS-s) mixed together. Now we take advantage of the background data. We let  $\tilde{X}$  be the protein expression from mice with genotype = control, which coincides with the background group used in previous studies of this application (Abid et al., 2018; Li et al., 2020). We set  $\tilde{Y}$  as the binary variable representing behavior and apply CPCA to  $(X, \tilde{X})$  and CIR to  $(X, Y, \tilde{X}, \tilde{Y})$  with  $d = 2$  as well. The 2-dimensional representations are shown in Figure 1, which indicates that CIR outperforms all other competitors. In particular, the three classes that were not separated in LDA are less mixed in CIR.

Next, we show the classification accuracy based on  $XV$ , the dimension-reduced data. Here, we vary  $d$  from 2 to 7 because for higher  $d$ , the accuracy is close to 1. The mean prediction accuracy of KNN, the best classifier for this example, over 10 replicates versus the reduced dimension  $d$  is shown in Figure 2, which clearly indicates that CIR outperforms all competitors especially when  $d$  is small. We present the accuracy of other classifiers and their standard deviations in Appendix G.1.

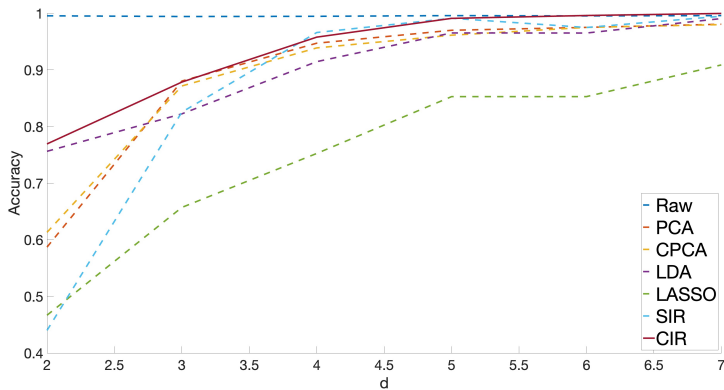


Figure 2: Classification accuracy by KNN for mouse protein data

## 4.2 Single Cell RNA Sequencing

The second dataset we considered is from a study of single-cell RNA sequencing used to classify cells into cell types based on their transcriptional profile Alquicira-Hernandez et al. (2019). The data include 3500 observations of expression levels of 32838 different genes, along with labels of the cell as one of 9 different cell types, namely CD8 T cell, CD4 T cell, classical monocyte, B cell, NK cell, plasmacytoid dendritic cell, non-classical monocyte, classic dendritic cell, and plasma cell. We select the top 100 most variable genes for our analysis to be consistent with previous analyses of these data Zheng et al. (2017); Abid et al. (2018). In this example,  $X \in \mathbb{R}^{3500 \times 100}$  represents the expression of 100 genes, while

$y_i \in \{0, 1, \dots, 8\}$  represents the cell type. For example,  $y_i = 1$  means that the  $i$ -th cell is a CD4 T cell.

To visualize the data, we apply unsupervised DR algorithms PCA, tSNE, and UMAP to  $X$  and supervised DR methods LDA, LASSO, and SIR to  $(X, Y)$ , for  $d = 2$  for all algorithms. In this case, there is no obvious choice of background data. So, we use  $\tilde{X} = X$  and randomly draw independent and identically distributed samples  $\tilde{Y} \sim \text{uniform}\{0, \dots, 8\}$  in order to apply CPCA and CIR. The 2-dimensional representation is given in Figure 3.

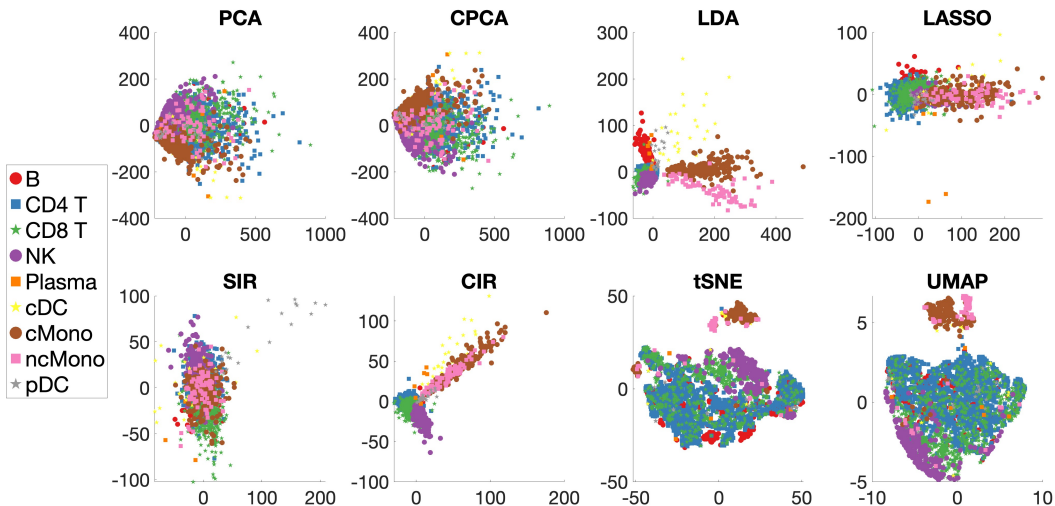


Figure 3: 2-d representation of single-cell RNA sequencing data

For each  $d = 2, \dots, 10$ , we compare the accuracy of a KNN classifier based on dimension-reduced data among various methods, with the raw data as the baseline. We repeat this process 10 times to reduce the impact of random split in cross-validation. The prediction accuracy versus reduced dimension  $d$  is shown in Figure 4, where CIR has the best overall performance especially when  $d = 2, 3$ . We show the accuracy of other classifiers and their standard deviations in Appendix G.2.

The improved performance of CIR over SIR deserves further comment. While the background data and labels  $(\tilde{X}, \tilde{Y})$  used in CIR do not add new information beyond what SIR used, because the background label is chosen randomly, we attribute the improved performance to CIR “denoising” the foreground data.

### 4.3 Plasma Retinol

The third dataset we consider is the plasma retinol dataset Nierenberg et al. (1989). The dataset contains 315 observations of 14 variables, including age, sex, smoking status, BMI,

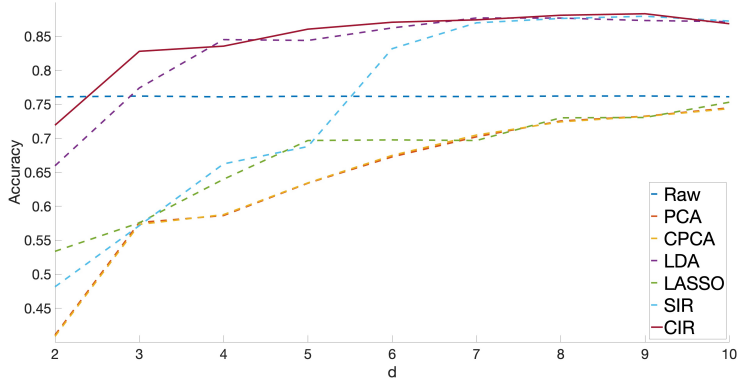


Figure 4: Classification accuracy by KNN for single-cell RNA sequencing data

vitamin use, calories, fat, fiber, cholesterol, dietary beta-carotene, dietary retinol consumed per day, number of alcoholic drinks consumed per week, and levels of plasma beta-carotene and plasma retinol.

In this example,  $X \in \mathbb{R}^{315 \times 12}$  represents measurements of the first 12 variables listed for all subjects, while  $y_i$  represents the measurement of plasma beta-carotene, a variable of particular interest to scientists Nierenberg et al. (1989). In contrast to the previous two examples, note that here  $y_i$  is continuous, not categorical.

We apply unsupervised DR algorithms PCA, tSNE, and UMAP to  $X$  and supervised DR algorithms LDA, LASSO, and SIR to  $(X, Y)$  for  $d = 1, \dots, 8$ . Similarly to the single-cell RNA sequencing application, we let  $\tilde{X} = X$  because there is no natural choice of background data. For the background label, we set  $\tilde{Y}$  as the continuous variable representing the level of plasma retinol, which shares certain information with  $y_i$ , and apply CPCA to  $(X, \tilde{X})$  and CIR to  $(X, Y, \tilde{X}, \tilde{Y})$  for  $d = 1, \dots, 8$ . We skip the visualization step in this case due to the poor visibility in terms of  $y_i$ .

After trying a few regression methods, namely linear regression Freedman (2009), regression trees Breiman et al. (2017), Gaussian process regression Chen et al. (2020), and neural networks Hopfield (1982), we present the prediction mean squared error (MSE) for the best method for this dataset, linear regression. That is, for each  $d$  and the output  $V$  from each DR algorithm, we fit a linear regression model to  $(XV, Y)$ . We also compare to a linear regression model based on raw data  $(X, Y)$  as the baseline. Figure 5 demonstrates that CIR outperforms all other competitors, but matches SIR when  $d \geq 3$ . We display the MSE of other regression methods and their standard deviations in Appendix G.3.

Note that because  $Y$  and  $\tilde{Y}$  are continuous, the number of slices to estimate  $\Sigma_x$  and  $\Sigma_{\tilde{x}}$  needs to be carefully chosen and adjusted to ensure optimal performance. We use cross-validation to select 4 equally spaced partitions for the support of  $Y$  and  $\tilde{Y}$ . In the three applications presented above, CIR demonstrates superior overall performance over its supervised,

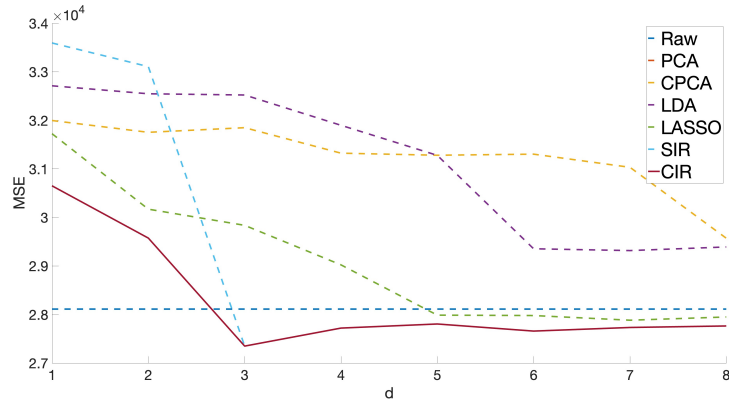


Figure 5: MSE of linear regression for plasma retinol data

unsupervised, contrastive, and non-contrastive competitors, especially in low dimension, i.e.,  $d = 2, 3$ , which are the most crucial dimensions for visualization purposes.

## 5 Discussion and Future Work

In this work, we propose the CIR model and the associated optimization algorithm for supervised dimension reduction for datasets that are split into foreground and background groups. We provide theoretical guarantee of the convergence of the CIR algorithm under mild conditions. We have shown that our CIR model outperforms competitors in multiple biomedical datasets, including mouse protein expression data, single-cell RNA sequencing data, and plasma retinol data. However, there are several important future directions that remain unaddressed in this paper, as outlined below.

**Multi-treatment.** It is natural to consider how our model can be extended to studies with multiple treatments. For example, in medical treatment, there might be more than one treatment for patients with certain disease. In Vogelstein et al. (2021), it has been shown that the number of treatment groups puts a hard constraint on the target dimension. It is interesting to generalize from a single-treatment structure to a multi-treatment structure (e.g., Luo and Strait (2022)), where the loss function needs more sophisticated design.

Another direction in multi-group scenario is to combine multiple CIR models trained on different pairs of bi-groups. As pointed out by Wolpert (1992), the generalization error in the contrastive regression model stacking needs to be controlled, and one possible way is to follow divergence mixing as proposed by Hinton (2002), with a careful normalization. The major difficulty in training such stacking model is how to devise a sequential optimization for model training.

**Consistency and sufficient dimension reduction.** The consistency of the proposed

CIR model remains open. Theorems 2 and 3 ensure that the resulting solution must be a stationary point, but we did not discuss whether these stationary points are consistent estimates. The consistency of the estimates is also affected by the choice of  $\alpha$ , because  $\alpha = 0$  will render this CIR into a classical SIR for the foreground group. This consistency problem also has practical importance, as it explicitly expresses the trade-off between the expressive contrastiveness and the emphasis on the effective lower-dimensional structures. The group information and statistical sufficiency compete against each other, as we observed in the experiments, thus a range of  $\alpha$  that balances between these two factors are of interest and might be answered by the consistency result.

Furthermore, SIR has the drawback of missing the totality central subspace when the symmetry assumption in  $x$  is lost (Li, 2018). Cook and Weisberg (1991) proposed the sliced average variance estimator (SAVE) estimator for addressing this problem, which raises the natural question of how to generalize this high-moment SDR method to the contrastive setting.

**Loss function.** Our loss function (4) is nonstandard, which raises many questions. For example, the relation between number of local minima and  $A, B, \tilde{A}, \tilde{B}, \alpha$  remains open. Moreover, although  $f$  cannot be continuously extended to the full Euclidean space  $\mathbb{R}^{p \times d}$ , if we restrict the domain to be a submanifold of  $\text{St}(p, d)$ ,  $f$  might be extended to the convex hull of the submanifold. This extension will enable us to apply some other efficient optimization algorithms with strong theoretical guarantee Boumal et al. (2019). Furthermore, Appendix F raises the question of the validity of a fixed-point algorithm based on Riccati equations that may lead to a more efficient algorithm to minimize  $f$  without involving the gradient.

## References

- Abid, A., Zhang, M. J., Bagaria, V. K., and Zou, J. (2018). Exploring patterns enriched in a dataset with contrastive principal component analysis. *Nature communications*, 9(1):1–7.
- Absil, P.-A., Mahony, R., and Sepulchre, R. (2009). Optimization algorithms on matrix manifolds. In *Optimization Algorithms on Matrix Manifolds*. Princeton University Press.
- Alquicira-Hernandez, J., Sathe, A., Ji, H. P., Nguyen, Q., and Powell, J. E. (2019). scPred: accurate supervised method for cell-type classification from single-cell RNA-seq data. *Genome biology*, 20(1):1–17.
- Bader, G. D., Cary, M. P., and Sander, C. (2006). Pathguide: a pathway resource list. *Nucleic acids research*, 34:D504–D506.
- Becht, E., McInnes, L., Healy, J., Dutertre, C.-A., Kwok, I. W., Ng, L. G., Ginhoux, F., and Newell, E. W. (2019). Dimensionality reduction for visualizing single-cell data using UMAP. *Nature biotechnology*, 37(1):38–44.



- Bini, D. A., Iannazzo, B., Meini, B., and Poloni, F. (2008). Nonsymmetric algebraic Riccati equations associated with an M-matrix: recent advances and algorithms. In *Dagstuhl Seminar Proceedings*. Schloss Dagstuhl-Leibniz-Zentrum für Informatik.
- Boumal, N., Absil, P.-A., and Cartis, C. (2019). Global rates of convergence for nonconvex optimization on manifolds. *IMA Journal of Numerical Analysis*, 39(1):1–33.
- Breiman, L., Friedman, J. H., Olshen, R. A., and Stone, C. J. (2017). *Classification and regression trees*. Routledge.
- Cai, Z., Li, R., and Zhu, L. (2020). Online sufficient dimension reduction through sliced inverse regression. *J. Mach. Learn. Res.*, 21(10):1–25.
- Camastra, F. and Staiano, A. (2016). Intrinsic dimension estimation: Advances and open problems. *Information Sciences*, 328:26–41.
- Campadelli, P., Casiraghi, E., Ceruti, C., and Rozza, A. (2015). Intrinsic dimension estimation: Relevant techniques and a benchmark framework. *Mathematical Problems in Engineering*, 2015.
- Chen, Z., Wang, B., and Gorban, A. N. (2020). Multivariate Gaussian and student-t process regression for multi-output prediction. *Neural Computing and Applications*, 32(8):3005–3028.
- Cook, R. D. (2009). *Regression graphics: Ideas for studying regressions through graphics*. John Wiley & Sons.
- Cook, R. D. and Weisberg, S. (1991). Sliced inverse regression for dimension reduction: Comment. *Journal of the American Statistical Association*, 86(414):328–332.
- Edelman, A., Arias, T. A., and Smith, S. T. (1998). The geometry of algorithms with orthogonality constraints. *SIAM journal on Matrix Analysis and Applications*, 20(2):303–353.
- Freedman, D. A. (2009). *Statistical models: theory and practice*. cambridge university press.
- Girard, S., Lorenzo, H., and Saracco, J. (2022). Advanced topics in sliced inverse regression. *Journal of Multivariate Analysis*, 188:104852.
- Hastie, T., Tibshirani, R., and Buja, A. (1994). Flexible discriminant analysis by optimal scoring. *Journal of the American statistical association*, 89(428):1255–1270.
- Higuera, C., Gardiner, K. J., and Cios, K. J. (2015). Self-organizing feature maps identify proteins critical to learning in a mouse model of Down syndrome. *PloS one*, 10(6):e0129126.

- Hilafu, H. and Safo, S. E. (2022). Sparse sliced inverse regression for high dimensional data analysis. *BMC bioinformatics*, 23(1):1–19.
- Hinton, G. E. (2002). Training products of experts by minimizing contrastive divergence. *Neural computation*, 14(8):1771–1800.
- Hopfield, J. J. (1982). Neural networks and physical systems with emergent collective computational abilities. *Proceedings of the national academy of sciences*, 79(8):2554–2558.
- Hotelling, H. (1992). Relations between two sets of variates. In *Breakthroughs in statistics*, pages 162–190. Springer.
- Hsing, T. and Carroll, R. J. (1992). An asymptotic theory for sliced inverse regression. *The Annals of Statistics*, pages 1040–1061.
- Jiang, C.-R., Yu, W., and Wang, J.-L. (2014). Inverse regression for longitudinal data. *The Annals of Statistics*, 42(2):563–591.
- Jones, A., Townes, F. W., Li, D., and Engelhardt, B. E. (2022). Contrastive latent variable modeling with application to case-control sequencing experiments. *The Annals of Applied Statistics*, 16(3):1268–1291.
- Li, B. (2018). *Sufficient dimension reduction: Methods and applications with R*. Chapman and Hall/CRC.
- Li, D., Jones, A., and Engelhardt, B. (2020). Probabilistic contrastive principal component analysis. *arXiv preprint arXiv:2012.07977*.
- Li, D., Mukhopadhyay, M., and Dunson, D. B. (2022). Efficient manifold approximation with spherelets. *Journal of the Royal Statistical Society Series B*, 84(4):1129–1149.
- Li, K.-C. (1991). Sliced inverse regression for dimension reduction. *Journal of the American Statistical Association*, 86(414):316–327.
- Li, L., Simonoff, J. S., and Tsai, C.-L. (2007). Tobit model estimation and sliced inverse regression. *Statistical Modelling*, 7(2):107–123.
- Li, L. and Yin, X. (2008). Sliced inverse regression with regularizations. *Biometrics*, 64(1):124–131.
- Liao, Y.-t., Luo, H., and Ma, A. (2023). Efficient Bayesian selection of hyper-parameters for dimension reduction: Case studies for t-SNE and UMAP. *In preparation*.
- Lin, Q., Zhao, Z., and Liu, J. S. (2018). On consistency and sparsity for sliced inverse regression in high dimensions. *The Annals of Statistics*, 46(2):580–610.

- Luo, H. and Li, D. (2022). Spherical rotation dimension reduction with geometric loss functions. *arXiv:2204.10975*, pages 1–56.
- Luo, H. and Strait, J. D. (2022). Nonparametric multi-shape modeling with uncertainty quantification. *arXiv preprint arXiv:2206.09127*.
- Nierenberg, D. W., Stukel, T. A., Baron, J. A., Dain, B. J., Greenberg, E. R., and Group, S. C. P. S. (1989). Determinants of plasma levels of beta-carotene and retinol. *American Journal of Epidemiology*, 130(3):511–521.
- Oviedo, H. and Dalmau, O. (2019). A scaled gradient projection method for minimization over the Stiefel manifold. In *Mexican International Conference on Artificial Intelligence*, pages 239–250. Springer.
- Tibshirani, R. (1996). Regression shrinkage and selection via the lasso. *Journal of the Royal Statistical Society: Series B (Methodological)*, 58(1):267–288.
- Van der Maaten, L. and Hinton, G. (2008). Visualizing data using t-SNE. *Journal of machine learning research*, 9(11).
- Virta, J., Lee, K.-Y., and Li, L. (2022). Sliced inverse regression in metric spaces. *arXiv preprint arXiv:2206.11511*.
- Vogelstein, J. T., Bridgeford, E. W., Tang, M., Zheng, D., Douville, C., Burns, R., and Maggioni, M. (2021). Supervised dimensionality reduction for big data. *Nature communications*, 12(1):1–9.
- Wilkinson, L. and Luo, H. (2022). A distance-preserving matrix sketch. *Journal of Computational and Graphical Statistics*, pages 1–15.
- Wolpert, D. H. (1992). Stacked generalization. *Neural networks*, 5(2):241–259.
- Wu, Q., Liang, F., and Mukherjee, S. (2013). Kernel sliced inverse regression: Regularization and consistency. In *Abstract and Applied Analysis*, volume 2013. Hindawi.
- Wu, Q., Mukherjee, S., and Liang, F. (2008). Localized sliced inverse regression. *Advances in neural information processing systems*, 21.
- Zheng, G. X., Terry, J. M., Belgrader, P., Ryvkin, P., Bent, Z. W., Wilson, R., Ziraldo, S. B., Wheeler, T. D., McDermott, G. P., Zhu, J., et al. (2017). Massively parallel digital transcriptional profiling of single cells. *Nature communications*, 8(1):1–12.
- Zou, J. Y., Hsu, D. J., Parkes, D. C., and Adams, R. P. (2013). Contrastive learning using spectral methods. *Advances in Neural Information Processing Systems*, 26.

## A Proof to Lemma 1

$$-\frac{\partial f}{\partial V} = 2AV(V^\top BV)^{-1} - 2BV(V^\top BV)^{-1}V^\top AV(V^\top BV)^{-1} \\ - \alpha \left\{ 2\tilde{A}V(V^\top \tilde{B}V)^{-1} - 2\tilde{B}V(V^\top \tilde{B}V)^{-1}V^\top \tilde{A}V(V^\top \tilde{B}V)^{-1} \right\}.$$

Recall that the projection to tangent space of the Stiefel manifold  $\text{St}(p, d)$  at  $V$  is given by

$$\text{Proj}_V(Z) = Z - V \text{Sym}(V^\top Z), \quad \forall Z \in T_V \text{St}(p, d),$$

where  $\text{Sym}(X) \cdots \frac{X+X^\top}{2}$  is the symmetrizer. Then observe that the following equations involving the pair  $A, B$  and the pair  $\tilde{A}, \tilde{B}$  have to satisfy the following equations:

$$V^\top \left( 2AV(V^\top BV)^{-1} - 2BV(V^\top BV)^{-1}V^\top AV(V^\top BV)^{-1} \right) = 0 \\ V^\top \left( 2\tilde{A}V(V^\top \tilde{B}V)^{-1} - 2\tilde{B}V(V^\top \tilde{B}V)^{-1}V^\top \tilde{A}V(V^\top \tilde{B}V)^{-1} \right) = 0.$$

That is,  $V^\top \frac{\partial f}{\partial V} = 0$ . As a result, the gradient of  $f$  is given by

$$-\text{grad } f(V) = \text{Proj}_V\left(\frac{\partial f}{\partial V}\right) = \frac{\partial f}{\partial V} - V \text{Sym}(V^\top \frac{\partial f}{\partial V}) = -\frac{\partial f}{\partial V}.$$

## B Proof of Theorem 1

If  $V$  is a local minimizer (i.e., a stationary point for the optimization problem (4)), then  $\text{grad } f(V) = 0$ , from Lemma 1 we have

$$AVE(V) - \alpha \tilde{A}V\tilde{E}(V) = BVF(V) - \alpha \tilde{B}V\tilde{F}(V),$$

where  $E(V) = (V^\top BV)^{-1}$ ,  $\tilde{E}(V) = (V^\top \tilde{B}V)^{-1}$ ,  $F(V) = (V^\top BV)^{-1}V^\top AV(V^\top BV)^{-1}$  and  $\tilde{F}(V) = (V^\top \tilde{B}V)^{-1}V^\top \tilde{A}V(V^\top \tilde{B}V)^{-1}$ .

## C Proof of Theorem 2

By Theorem 1 and Corollary 1 in Oviedo and Dalmau (2019), it suffices to show  $f$  is continuously differentiable, which is a directly corollary of Lemma 1.

## D Options for $\eta_k$

To introduce other options for  $\eta_k$ , we need the following definition.

**Definition 3.** (*Gradient-related sequence, see Absil et al. (2009) (p.62, Definition 4.2.1)*). Given a function  $f$  on a Riemannian manifold  $M$ , a sequence in tangent space  $\{\eta_k\}, \eta_k \in T_{V_k}M$ , where  $V_k$  are defined through the iterative formula  $V_{k+1} = R_{V_k}(t_k \eta_k)$ , and  $R_{x_k}$  can be any retraction (e.g., global retraction mapping  $\text{Retr}_V : T_V M \rightarrow M, \xi \mapsto (V + \xi)(I_d + \xi^\top \xi)^{-1/2}$  on  $\text{St}(n, p)$ ), is called **gradient-related** if, for any subsequence of  $\{V_k\}_{k \in K \subset \{1, 2, \dots, n\}}$  that converges to a non-critical point of  $f$ , the corresponding subsequence  $\{\eta_k\}_{k \in K}$  is bounded and satisfies

$$\lim_{k \rightarrow \infty} \sup_{k \in K} \langle \text{grad } f(V_k), \eta_k \rangle_M < 0.$$

This means that the cosine of gradient and update  $\eta_k$  needs to form an acute angle for only critical points. Note that a naive Newton step is not necessarily gradient-related (see p.122 in Absil et al. (2009)). In particular,  $\eta_k = -\text{grad } f(V_k)$  results in a gradient-related sequence, and is suggested by Absil et al. (2009) as a natural choice.

## E Proof of Theorem 3

The first assertion regarding consistency is from Theorem 4.3.1 in Absil et al. (2009), which requires our loss function  $f$  to be continuously differentiable, a direct corollary of Lemma 1.

By the compactness of  $\text{St}(p, d)$ , the level set  $\mathcal{L} := \{V \in \text{St}(p, d) : f(V) \leq f(V_0)\}$  is compact for any  $V_0 \in \text{St}(p, d)$ , the second assertion follows Corollary 4.3.2 in Absil et al. (2009).

The third assertion regarding convergence rate involves second-order conditions, i.e., the Hessian of  $f$ . Let  $D^2 f$  be the Hessian computed in Euclidean coordinates, that is,  $(D^2 f|_V)_{ij,kl} := \frac{\partial^2 f}{\partial V_{ij} \partial V_{kl}}$ , then for tangent vectors  $\Omega_1, \Omega_2 \in T_V \text{St}(p, d)$ , the Hessian is given by Absil et al. (2009)

$$\begin{aligned} \text{Hess}(f)(\Omega_1, \Omega_2) = & \underbrace{D^2 f|_V(\Omega_1, \Omega_2)}_{\textcircled{1}} + \underbrace{\frac{1}{2} \text{tr} \left( (\text{grad } f(V)^\top \Omega_1 V^\top + V^\top \Omega_1 \text{grad } f(V)^\top) \Omega_2 \right)}_{\textcircled{2}} \\ & - \underbrace{\frac{1}{2} \text{tr} \left( (V^\top \text{grad } f(V) + \text{grad } f(V)^\top V) \Omega_1^\top (I_p - VV^\top) \Omega_2 \right)}_{\textcircled{3}}. \end{aligned}$$

By the definition of  $f$ ,  $\textcircled{1}$  is  $C^\infty$  in the Euclidean sense, so is continuous. By the continuity of  $\text{grad } f$ ,  $\textcircled{2}$  and  $\textcircled{3}$  are also continuous since they are product or summation of continuous functions. Then the convergence rate follows Theorem 4.5.6 in Absil et al. (2009).

## F Fixed-Point Approach to Optimization

Motivated by the first order optimality condition for the loss function (4), we seek a fixed-point method as an alternative to a gradient descent-based algorithm. Instead of solving equation (5) in one algebraic step, we separate the problem into the following 8 equations, which can be solved cyclically. Recall that  $E(V) = (V^\top BV)^{-1}$ ,  $\tilde{E}(V) = (V^\top \tilde{B}V)^{-1}$ ,  $G(V) = V^\top AV$ , and  $\tilde{G}(V) = V^\top \tilde{A}V$  and suppress the index of  $V_k$ , i.e.,  $V = V_k$  for now for legibility:

$$AV_{k+1}E(V) - \alpha\tilde{A}V\tilde{E}(V) = BVE(V)G(V)E(V) - \alpha\tilde{B}V\tilde{E}(V)\tilde{G}(V)\tilde{E}(V) \quad (6)$$

$$AVE(V) - \alpha\tilde{A}V_{k+1}\tilde{E}(V) = BVE(V)G(V)E(V) - \alpha\tilde{B}V\tilde{E}(V)\tilde{G}(V)\tilde{E}(V) \quad (7)$$

$$AVE(V) - \alpha\tilde{A}V\tilde{E}(V) = BV_{k+1}E(V)G(V)E(V) - \alpha\tilde{B}V\tilde{E}(V)\tilde{G}(V)\tilde{E}(V) \quad (8)$$

$$AVE(V) - \alpha\tilde{A}V\tilde{E}(V) = BVE(V)G(V)E(V) - \alpha\tilde{B}V_{k+1}\tilde{E}(V)\tilde{G}(V)\tilde{E}(V) \quad (9)$$

$$AVE(V_{k+1}) - \alpha\tilde{A}V\tilde{E}(V) = BVE(V_{k+1})G(V)E(V_{k+1}) - \alpha\tilde{B}V\tilde{E}(V)\tilde{G}(V)\tilde{E}(V) \quad (10)$$

$$AVE(V) - \alpha\tilde{A}V\tilde{E}(V_{k+1}) = BVE(V)G(V)E(V) - \alpha\tilde{B}V\tilde{E}(V_{k+1})\tilde{G}(V)\tilde{E}(V_{k+1}) \quad (11)$$

$$AVE(V) - \alpha\tilde{A}V\tilde{E}(V) = BVE(V)G(V_{k+1})E(V) - \alpha\tilde{B}V\tilde{E}(V)\tilde{G}(V)\tilde{E}(V) \quad (12)$$

$$AVE(V) - \alpha\tilde{A}V\tilde{E}(V) = BVE(V)G(V)E(V) - \alpha\tilde{B}V\tilde{E}(V)\tilde{G}(V_{k+1})\tilde{E}(V) \quad (13)$$

In each of the first four of these equations,  $V_{k+1}$  can change independently, suggesting a convenient corresponding update rule. For the next two equations, we can premultiply by  $[(BV)^\top(BV)]^{-1}(BV)^\top$  (and  $[(\tilde{B}V)^\top(\tilde{B}V)]^{-1}(\tilde{B}V)^\top$ , respectively) to obtain the following equation:

$$\left[(BV)^\top(BV)\right]^{-1}(BV)^\top AVE(V_{k+1}) - E(V_{k+1})G(V)E(V_{k+1}) = \alpha \left[(BV)^\top(BV)\right]^{-1}(BV)^\top H_1, \quad (14)$$

where  $H_1 = \left(\tilde{A}V\tilde{E}(V) - \tilde{B}V\tilde{E}(V)\tilde{G}(V)\tilde{E}(V)\right)$ .

In practice, the cyclic update may not converge to stationary points of the optimization problem (4). However, when the designated cyclic update converges, it can be shown that equation (14) is in the form of an asymmetric algebraic Riccati equation in  $E(V_{k+1})$  Bini et al. (2008). When we obtain a solution  $E^* = E(V_{k+1})$  where  $V = V_k$  is not a local optimum, the  $E^*$  is not in  $S_{++}^d$ , which means we cannot use the Cholesky decomposition to solve for  $V_{k+1}$  in the next update.

For the final two equations, we can write

$$V_{k+1}^\top AV_{k+1} = \left[(VE(V))^\top(VE(V))\right]^{-1} (VE(V))^\top B^{-1} H_2 E(V)^{-1},$$

where  $H_2 = AVE(V) + \alpha \left(\tilde{B}V\tilde{E}(V)\tilde{G}(V)\tilde{E}(V) - \tilde{A}V\tilde{E}(V)\right)$ . However, when  $V = V_k$  is not a local optimum, again the right-hand side is not symmetric positive-definite, and so we cannot use the Cholesky decomposition to solve for  $V_{k+1}$  in the next update.

Note that in order to require  $V_{k+1} \in \text{St}(p, d)$ , the final step of each update rule should project the solution for  $V_{k+1}$  onto  $\text{St}(p, d)$ , which can be done via SVD; if  $A = U\Sigma V^\top$ , then  $\pi(A) = UV^\top$ .

Although this cyclic update regime does not immediately lead to a practical fixed-point optimization algorithm, it shows that our loss function has the classical link to a Ricatti equation (14), indicating more efficient algorithms are possible.

## G Additional experimental details

We provide more details about empirical studies in Section 4. There are three main purposes of this appendix.

1. We provide classification accuracy or prediction MSE from multiple commonly used algorithms since the true function  $\varphi$  can be arbitrary in Equation (3).
2. We provide the standard deviation that results from random split in cross validation with 10 replicates.
3. We provide the time of 8 DR algorithms: PCA, CPCA, LDA, LASSO, SIR CIR, tSNE and UMAP with  $d = 2$ . The run time is based on an personal iMac 2021 with M1 chip.

### G.1 Mouse protein

We first compare the run time for 8 DR algorithms. Note that contrastive models take 552 foreground samples along with 255 background samples so the total sample size is 807, while non-contrastive models take only 552 samples. In contrast, unsupervised methods take 77 input features, i.e., 77 proteins, while supervised method take one additional feature, the response variable  $y$  into consideration so  $p = 77 + 1 = 78$ .

Table 3: Time (seconds) of DR methods on mouse protein data

	n	p	d	time
PCA	552	77	2	0.01
CPCA	807	77	2	0.01
LDA	552	78	2	0.02
LASSO	552	78	2	0.05
SIR	552	78	2	0.05
CIR	807	78	2	1.16
tSNE	552	77	2	0.62
UMAP	552	77	2	5.31

We present the classification accuracy by KNN, trees, SVM, boosting and neural network applied to mouse protein data. All models are trained by the MATLAB app: classification learner. The reduced dimension  $d = 2, 3, \dots, 7$  because when  $d > 7$  the accuracy from almost all methods is close to 1. We removed the standard deviation for those less than 0.0001 for simplicity.

Table 4: Classification accuracy (standard deviation) of KNN for different DR methods and  $d$

DR \ d	2	3	4	5	6	7
raw	0.996(0)	0.996(0)	0.996(0)	0.995(0)	0.994(0)	0.995(0)
PCA	0.588(0.01)	0.881(0.01)	0.945(0)	0.971(0)	0.974(0)	0.979(0.01)
CPCA	0.614(0.01)	0.880(0.01)	0.933 (0.01)	0.959(0.01)	0.973(0.01)	0.978(0.01)
LDA	0.754(0.01)	0.821(0.01)	0.911(0)	0.966(0)	0.966 (0)	0.991(0)
LASSO	0.464 (0.01)	0.661(0.01)	0.753(0.01)	0.859 (0.01)	0.853(0)	0.911(0.01)
SIR	0.445(0.01)	0.826(0)	<b>0.965(0)</b>	<b>0.991(0)</b>	0.974(0)	<b>0.996(0)</b>
CIR	<b>0.772(0)</b>	<b>0.914(0)</b>	0.958(0)	0.990(0)	<b>0.997(0)</b>	0.995(0.01)

Table 5: Classification accuracy (standard deviation) of trees for different DR methods and  $d$

DR \ d	2	3	4	5	6	7
raw	0.890(0.01)	0.889(0.01)	0.890(0.01)	0.890(0.01)	0.886(0.01)	0.884(0.01)
PCA	0.427(0.02)	0.703(0.02)	0.805(0.01)	0.819(0.01)	0.846(0.01)	0.850(0.01)
CPCA	0.463(0.02)	0.671(0.02)	0.718(0.01)	0.721(0.02)	0.759(0.01)	0.767(0.01)
LDA	<b>0.785(0.01)</b>	<b>0.879(0.01)</b>	<b>0.939(0)</b>	<b>0.986(0)</b>	<b>0.992(0)</b>	0.989(0)
LASSO	0.454(0.01)	0.576(0.01)	0.690(0.01)	0.78(0.01)	0.770(0.01)	0.794(0.02)
SIR	0.482(0.01)	0.817(0.01)	0.941(0.01)	0.981(0)	0.983(0)	<b>0.992(0)</b>
CIR	0.759(0.01)	0.863(0.01)	0.906(0.01)	0.912(0.01)	0.954(0.01)	0.874(0.01)

For  $d = 2, 3$  and various choices of  $\alpha$ , we present KNN classification accuracy on this dataset. The small changes in  $\alpha$  support the claim that CIR is robust in  $\alpha$ . For  $d = 2$ , we provide the corresponding visualizations.



Table 6: Classification accuracy (standard deviation) of SVM for different DR methods and  $d$

DR \ d	2	3	4	5	6	7
raw	0.993(0)	0.993(0)	0.993(0)	0.993(0)	0.992(0)	0.994(0)
PCA	0.329(0.01)	0.596(0.01)	0.742(0)	0.803(0.01)	0.825(0)	0.846(0)
CPCA	0.415(0.04)	0.542(0.01)	0.650(0.01)	0.749(0.01)	0.782(0)	0.788(0)
LDA	0.426(0)	0.426(0)	0.426(0)	0.428(0)	0.428(0)	0.428(0)
LASSO	0.163(0)	0.179(0)	0.350(0.01)	0.505(0.01)	0.502(0.01)	0.506(0.01)
SIR	0.163(0)	0.163(0)	0.163(0)	0.163(0)	0.242(0)	0.246(0)
CIR	<b>0.749(0)</b>	<b>0.849(0)</b>	<b>0.882(0)</b>	<b>0.876(0)</b>	<b>0.942(0)</b>	<b>0.924(0)</b>

Table 7: Classification accuracy (standard deviation) of boosting for different DR methods and  $d$

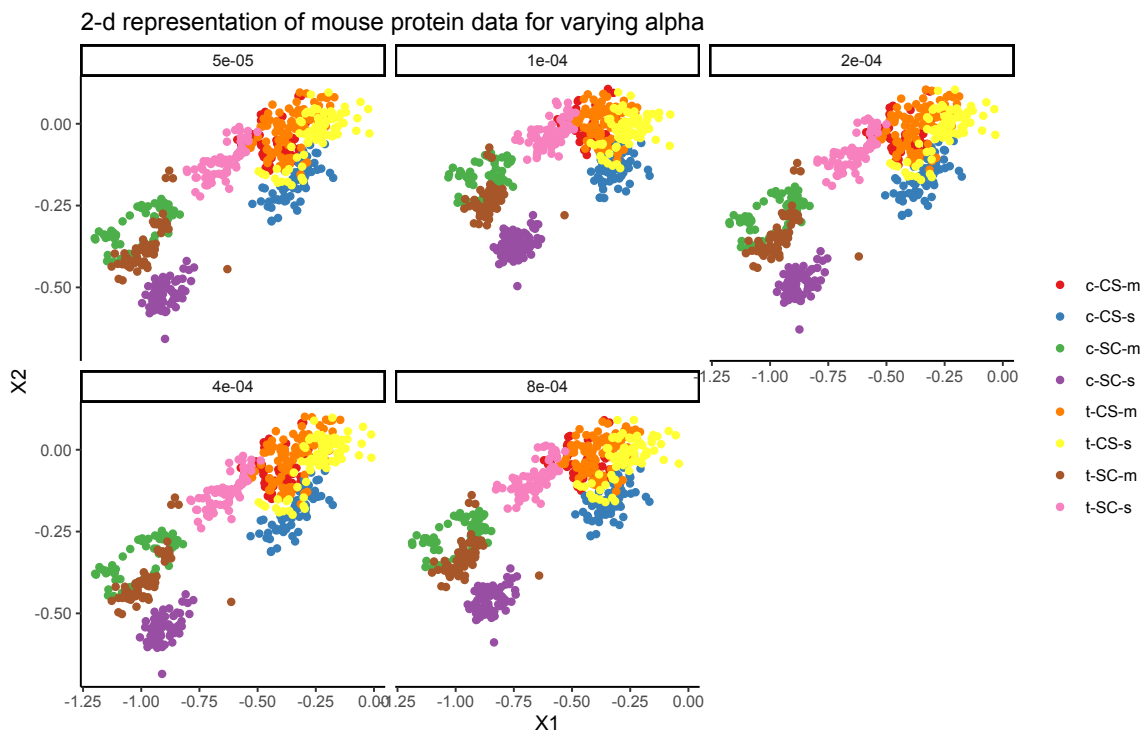
DR \ d	2	3	4	5	6	7
raw	0.986(0)	0.985(0)	0.984(0)	0.988(0)	0.985(0)	0.986(0)
PCA	0.408(0.01)	0.607(0.01)	0.754(0.01)	0.822(0.01)	0.872(0.01)	0.898(0.01)
CPCA	0.452(0.01)	0.680(0.01)	0.744(0.01)	0.796(0.01)	0.858(0.01)	0.870(0.01)
LDA	<b>0.790(0.01)</b>	<b>0.900(0.01)</b>	0.950(0)	0.875(0.06)	0.0815(0)	0.08152(0)
LASSO	0.474(0.01)	0.520(0.01)	0.711(0.01)	0.805(0.01)	0.812(0.01)	0.842(0.01)
SIR	0.544(0.01)	0.840(0.01)	<b>0.964(0.01)</b>	<b>0.981(0.03)</b>	0.953(0.05)	0.082(0)
CIR	0.787(0.01)	0.866(0.01)	0.945(0.04)	0.948(0)	<b>0.977(0)</b>	<b>0.973(0)</b>

Table 8: Classification accuracy (standard deviation) of neural network classifier for different DR methods and  $d$

DR \ d	2	3	4	5	6	7
raw	0.909(0.04)	0.903(0.06)	0.895(0.03)	0.898(0.03)	0.881(0.06)	0.901(0.04)
PCA	0.466(0.01)	0.798(0.02)	0.90(0.01)	0.924(0.01)	0.934(0.01)	0.943(0.01)
CPCA	0.560(0.01)	0.825(0.01)	0.860(0.01)	0.880(0.01)	0.924(0.01)	0.925(0.01)
LDA	<b>0.813(0.01)</b>	<b>0.877(0.01)</b>	0.926(0.02)	<b>0.968(0.02)</b>	0.976(0.01)	0.965(0.02)
LASSO	0.490(0.01)	0.490(0.03)	0.648(0.02)	0.803(0.02)	0.815(0.02)	0.863(0.01)
SIR	0.55(0.03)	0.835(0.02)	0.953(0.02)	0.964(0.02)	0.964(0.02)	<b>0.982(0)</b>
CIR	0.788(0.01)	0.871(0.01)	<b>0.939(0.01)</b>	0.951(0)	<b>0.978(0)</b>	0.979(0.01)

Table 9: Classification Accuracy (standard deviation) of KNN for CIR, with different  $\alpha$  and  $d = 2, 3$ .

d \ $\alpha$	$5 \cdot 10^{-5}$	$10^{-4}$	$2 \cdot 10^{-4}$	$4 \cdot 10^{-4}$	$8 \cdot 10^{-4}$
2	0.740 (0.0237)	0.775 (0.017)	0.751 (0.0338)	0.747 (0.0336)	0.753 (0.0244)
3	0.874 (0.0241)	0.860 (0.0122)	0.869 (0.0270)	0.867 (0.0306)	0.855 (0.0265)



## G.2 Single-cell RNA sequencing

We first compare the run time for 8 DR algorithms. Note that contrastive models take 3500 foreground samples along with 3500 background samples so the total sample size is 7000, while non-contrastive models take only 3500 samples. In contrast, unsupervised methods take 100 input features, i.e., 100 genes, while supervised method take one additional feature, the response variable  $y$  into consideration so  $p = 100 + 1 = 101$ .

We present the classification accuracy by KNN, trees, boosting and neural network applied to single-cell RNA sequencing data. We will not present the accuracy from SVM since the time is much higher than other classifiers, where a single training takes about 20 minutes (we have 10 replicates and 6 options for  $d$  so the total time will be 1200 minutes for SVM). All models are trained by the MATLAB app: classification learner. The reduced dimension  $d = 2, 3, \dots, 7$  because when  $d > 7$  the accuracy remains stable when  $d$  keeps increasing. We removed the standard deviation for those less than 0.0001 for simplicity.

For  $d = 2, 3$ ,  $p = 100, 200, 300, 400, 500$ , and various choices of  $\alpha$ , we present KNN classification accuracy on this dataset. The small changes in both  $\alpha$  and  $p$  support the claim that CIR is robust in  $\alpha$  and  $p$ . For  $d = 2$ , we provide the corresponding visualizations.

Table 10: Time (seconds) of DR methods on single-cell RNA sequencing data

	n	p	d	time
PCA	3500	100	2	0.03
CPCA	7000	100	2	0.04
LDA	3500	101	2	0.08
LASSO	3500	101	2	0.09
SIR	3500	101	2	0.06
CIR	7000	101	2	4.96
tSNE	3500	100	2	3.28
UMAP	3500	100	2	4.97

Table 11: Classification accuracy (standard deviation) of KNN for different DR methods and  $d$

DR \ d	2	3	4	5	6	7
raw	0.761(0)	0.761(0)	0.762(0)	0.762(0)	0.762(0)	0.762(0)
PCA	0.411(0)	0.577(0)	0.588(0)	0.635(0)	0.676(0)	0.704(0)
CPCA	0.412(0)	0.575(0)	0.587(0)	0.635(0)	0.676(0)	0.703(0)
LDA	0.659(0)	0.776(0)	<b>0.844(0)</b>	0.844(0)	0.862(0)	<b>0.877(0)</b>
LASSO	0.534(0)	0.577(0)	0.642(0)	0.697(0)	0.696(0)	0.697(0)
SIR	0.481(0.01)	0.570(0.01)	0.661(0)	0.690(0)	0.832(0)	0.871(0)
CIR	<b>0.711(0)</b>	<b>0.823(0)</b>	0.833(0)	<b>0.866(0)</b>	<b>0.864(0)</b>	0.876(0)

Table 12: Classification accuracy (standard deviation) of Trees for different DR methods and  $d$

DR \ d	2	3	4	5	6	7
raw	0.753(0.01)	0.758(0.01)	0.756(0.01)	0.756(0)	0.754(0.01)	0.755(0)
PCA	0.450(0.01)	0.590(0.01)	0.633(0.01)	0.653(0.01)	0.710(0)	0.731(0.01)
CPCA	0.448(0.01)	0.591(0)	0.634(0)	0.656(0.01)	0.716(0)	0.729(0)
LDA	0.676(0)	0.776(0)	<b>0.839(0)</b>	0.835(0)	0.840(0)	0.862(0)
LASSO	0.555(0.01)	0.585(0.01)	0.634(0.01)	0.692(0.01)	0.689(0.01)	0.690(0)
SIR	0.510(0.01)	0.603(0)	0.668(0.01)	0.685(0.01)	0.825(0.01)	0.859(0)
CIR	<b>0.721(0)</b>	<b>0.821(0.01)</b>	0.827(0)	<b>0.845(0)</b>	<b>0.853(0.01)</b>	<b>0.868(0)</b>

Table 13: Classification accuracy (standard deviation) of boosting for different DR methods and  $d$

DR \ d	2	3	4	5	6	7
raw	0.826(0)	0.827(0)	0.826(0)	0.828(0)	0.826(0)	0.827(0)
PCA	0.540(0)	0.689(0)	0.714(0)	0.722(0)	0.777(0)	0.794(0)
CPCA	0.539(0)	0.690(0)	0.714(0)	0.723(0)	0.779(0)	0.795(0)
LDA	0.747(0)	0.832(0)	<b>0.872(0)</b>	0.877(0)	0.876(0)	0.895(0)
LASSO	0.662(0)	0.692(0)	0.711(0)	0.769(0)	0.768(0)	0.768(0)
SIR	0.624(0)	0.688(0)	0.7419(0)	0.754(0)	0.864(0)	0.889(0)
CIR	<b>0.786(0)</b>	<b>0.858(0)</b>	0.868(0)	<b>0.882(0)</b>	<b>0.889(0)</b>	<b>0.896(0)</b>

Table 14: Classification accuracy (standard deviation) of neural network classifier for different DR methods and  $d$

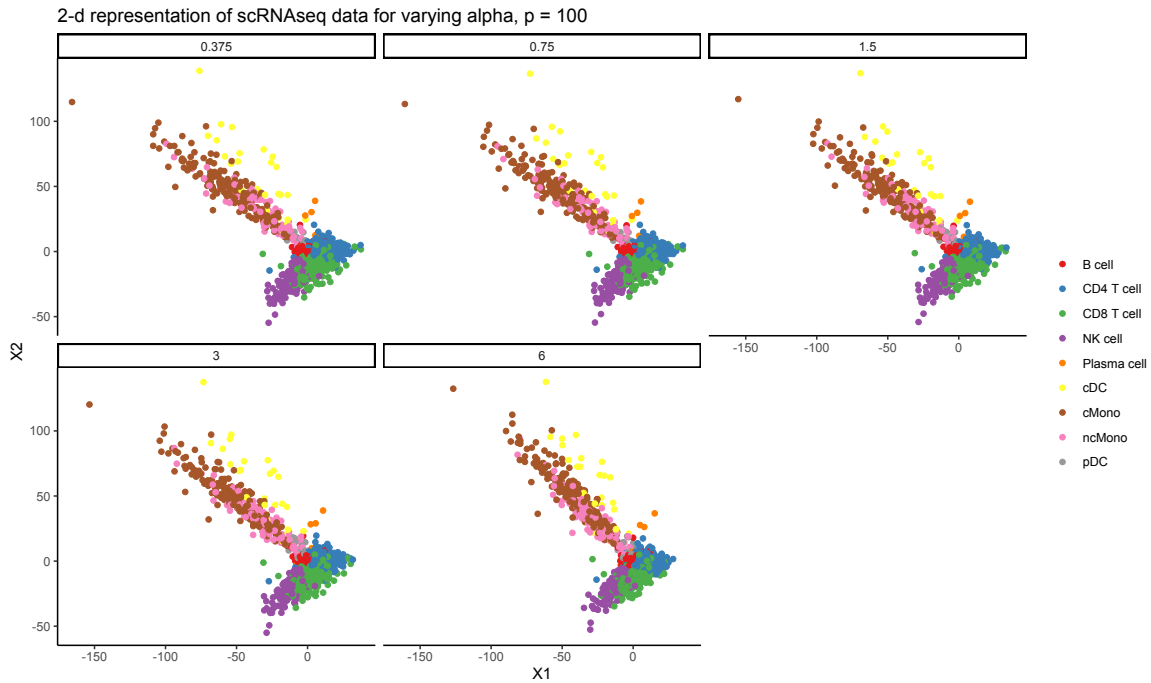
DR \ d	2	3	4	5	6	7
raw	0.870(0.01)	0.859(0.03)	0.870(0.0220)	0.867(0.02)	0.870(0.01)	0.870(0.02)
PCA	0.514(0.01)	0.671(0.02)	0.683(0.04)	0.725(0.02)	0.784(0.02)	0.794(0.03)
CPCA	0.506(0.01)	0.678(0.01)	0.705(0.03)	0.758(0.01)	0.782(0.03)	0.797(0.03)
LDA	0.748(0)	0.841(0)	<b>0.886(0)</b>	0.886(0)	0.886(0)	0.904(0)
LASSO	0.661(0)	0.697(0)	0.757(0)	0.790(0)	0.789(0)	0.789(0)
SIR	0.628(0)	0.701(0)	0.754(0)	0.771(0)	0.878(0)	0.898(0)
CIR	<b>0.796(0)</b>	<b>0.880(0)</b>	0.881(0)	<b>0.890(0)</b>	<b>0.903(0)</b>	<b>0.905(0)</b>

Table 15: Classification Accuracy (standard deviation) of KNN for CIR, with different  $\alpha$ ,  $p$  and  $d = 2$ .

$p$ \ $\alpha$	0.375	0.75	1.5	3	6
100	0.747 (0.015)	0.741 (0.019)	0.742 (0.026)	0.722 (0.011)	0.707 (0.018)
200	0.766 (0.006)	0.771 (0.012)	0.764 (0.019)	0.741 (0.007)	0.718 (0.008)
300	0.777 (0.006)	0.770 (0.013)	0.773 (0.006)	0.756 (0.007)	0.720 (0.006)
400	0.779 (0.011)	0.775 (0.006)	0.777 (0.015)	0.763 (0.015)	0.724 (0.008)
500	0.785 (0.008)	0.783 (0.015)	0.784 (0.016)	0.762 (0.017)	0.727 (0.012)

Table 16: Classification Accuracy (standard deviation) of KNN for CIR, with different  $\alpha$ ,  $p$  and  $d = 3$ .

$\alpha \backslash p$	0.375	0.75	1.5	3	6
100	0.810 (0.010)	0.813 (0.005)	0.810 (0.010)	0.794 (0.012)	0.760 (0.008)
200	0.841 (0.012)	0.854 (0.003)	0.842 (0.011)	0.828 (0.006)	0.808 (0.008)
300	0.865 (0.009)	0.854 (0.005)	0.862 (0.013)	0.838 (0.004)	0.806 (0.003)
400	0.861 (0.007)	0.857 (0.008)	0.850 (0.013)	0.834 (0.005)	0.812 (0.005)
500	0.867 (0.007)	0.858 (0.005)	0.853 (0.011)	0.848 (0.013)	0.816 (0.007)

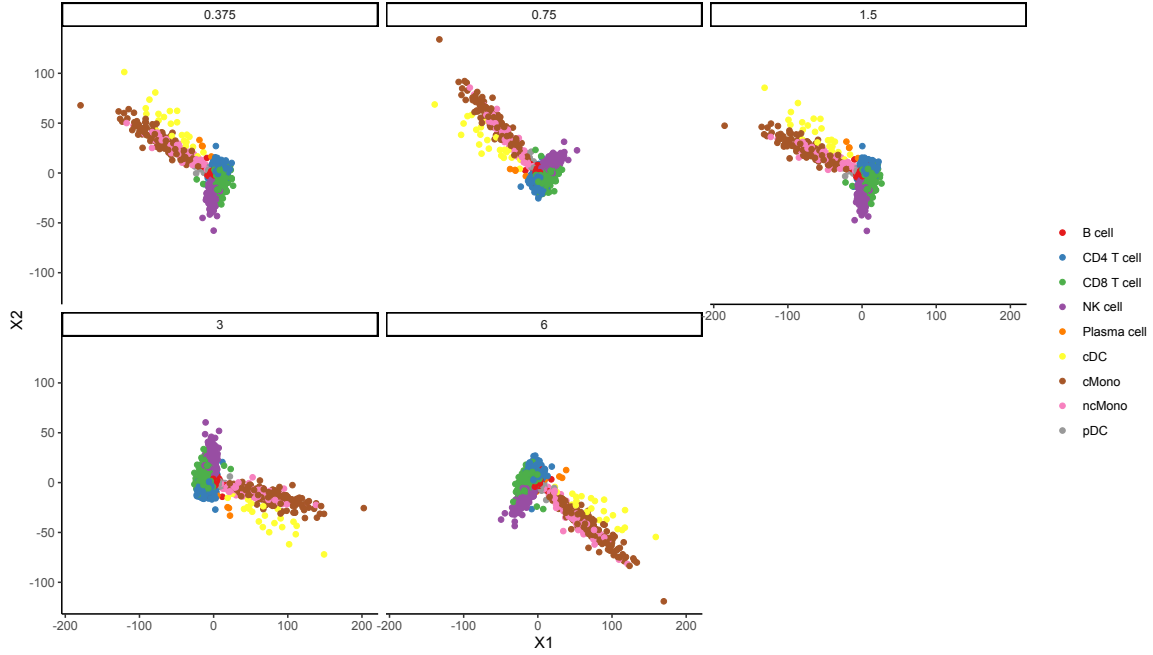


### G.3 Plasma retinol

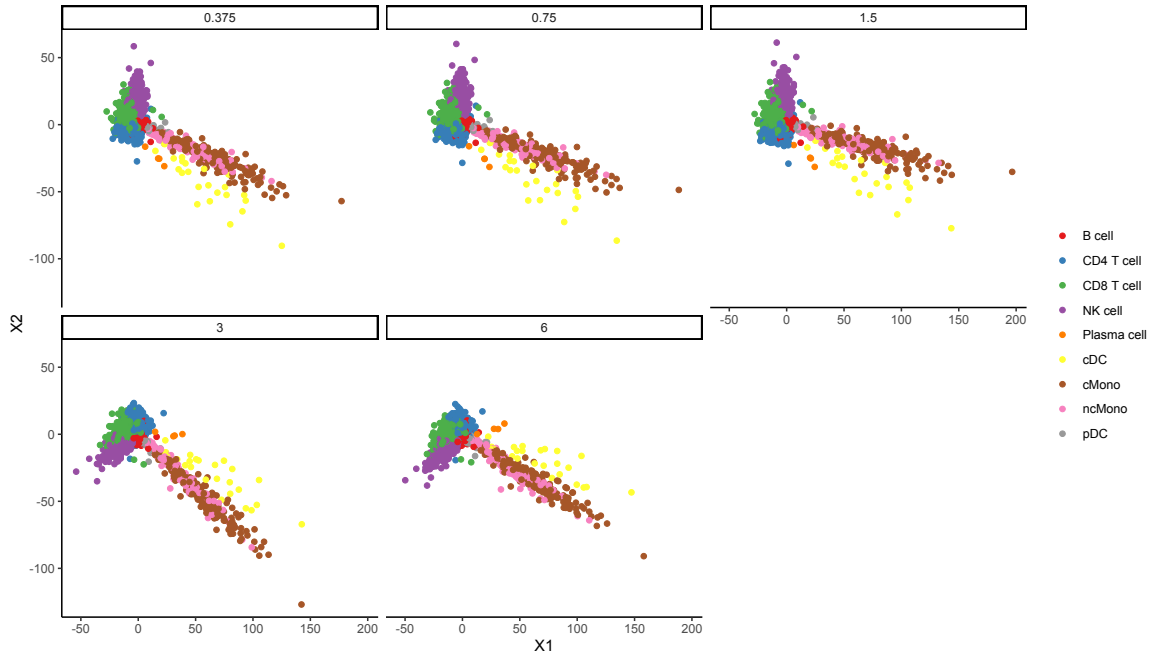
We first compare the run time for 8 DR algorithms. Note that contrastive models take 315 foreground samples along with 315 background samples so the total sample size is 630, while non-contrastive models take only 315 samples. In contrast, unsupervised methods take 12 input features, while supervised method take one additional feature, the response variable  $y$  into consideration so  $p = 12 + 1 = 13$ .

We present the regression MSE by linear regression, trees, SVM, GP and neural network applied to plasma retinol data. All models are trained by the MATLAB app: regression learner. The reduced dimension  $d = 1, 2, \dots, 8$  because when  $d > 8$  MSE will not change

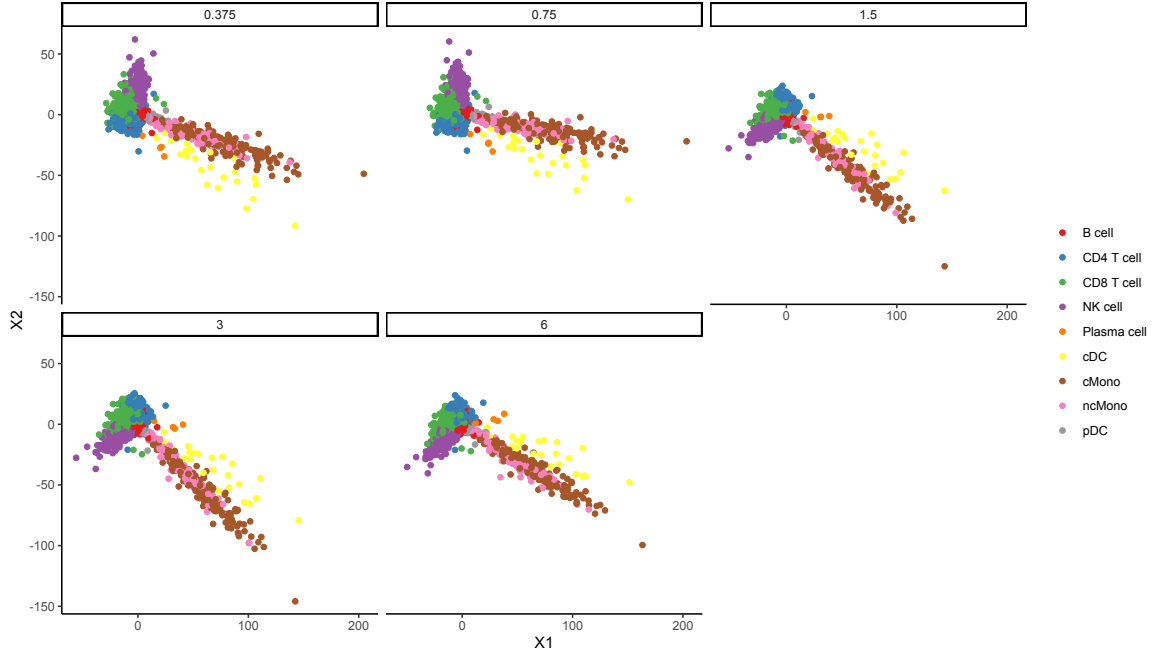
2-d representation of scRNAseq data for varying alpha,  $p = 200$



2-d representation of scRNAseq data for varying alpha,  $p = 300$



2-d representation of scRNAseq data for varying alpha,  $p = 400$



2-d representation of scRNAseq data for varying alpha,  $p = 500$

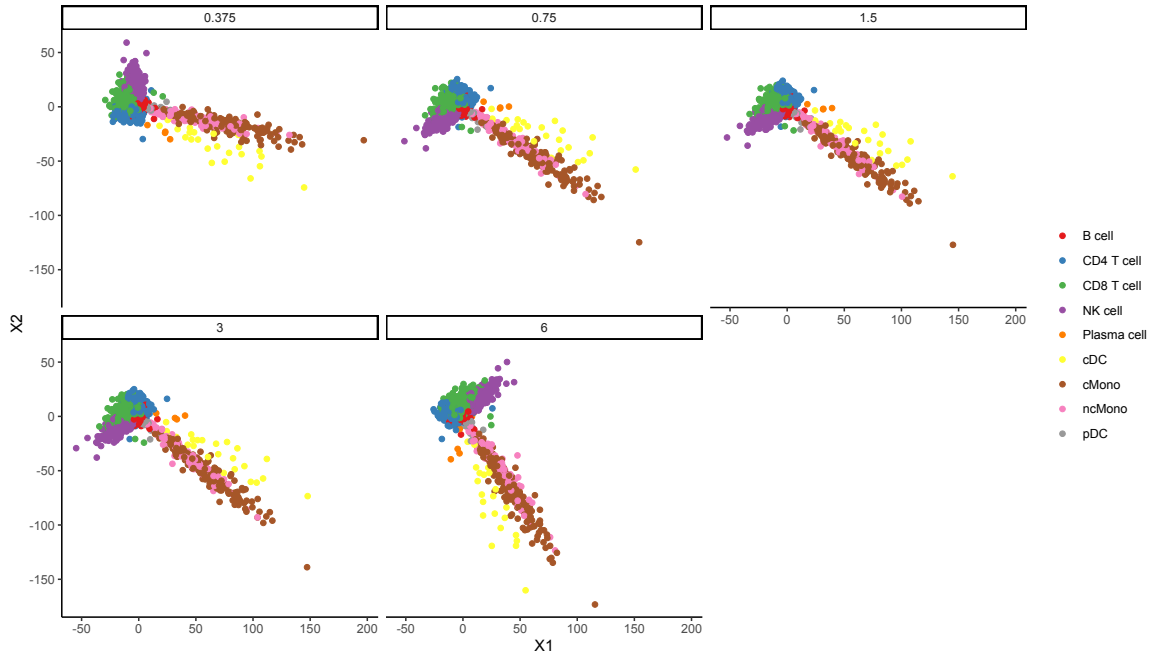




Table 17: Time (seconds) of DR methods on plasma retinol data

	n	p	d	time
PCA	315	12	2	0.02
CPCA	630	12	2	0.02
LDA	315	13	2	0.03
LASSO	315	13	2	0.05
SIR	552	13	2	0.05
CIR	630	13	2	0.21
tSNE	315	12	2	0.39
UMAP	315	12	2	4.16

significantly. We note that we removed the standard deviation for those less than 10 for simplicity.

Note that for table 18, the standard deviation of every entry is less than  $10^{-4}$ .

Table 18: Prediction MSE of linear regression for different DR methods and  $d$

DR \ d	1	2	3	4	5	6	7	8
raw	28112	28112	28112	28112	28112	28112	28112	28112
PCA	31997	31754	31850	31324	31282	31304	31033	29572
CPCA	31997	31754	31850	31324	31282	31304	31033	29572
LDA	32713	32548	32523	31899	31279	29354	29317	29392
LASSO	31725	<b>30170</b>	29837	29023	27987	27979	27882	27949
SIR	33595	33108	<b>27349</b>	<b>27720</b>	<b>27804</b>	<b>27658</b>	<b>27733</b>	<b>27764</b>
CIR	<b>30139</b>	30216	27833	<b>27720</b>	<b>27804</b>	<b>27658</b>	<b>27733</b>	<b>27764</b>

For table 22 (neural network regression), according to the baseline MSE from raw data, we replace the MSEs greater than 100000 or standard deviation greater than 10000 by \*, which might result from over-fitting.

Table 19: Prediction MSE/100 (standard deviation/100) of regression tree for different DR methods and  $d$

DR \ d	1	2	3	4	5	6	7	8
raw	515(32)	481(30)	476(37)	461(34)	462(42)	443(46)	469(34)	459(38)
PCA	519(42)	537(36)	532(78)	580(67)	592(55)	594(67)	581(50)	576(47)
CPCA	513(40)	555(64)	561(55)	565(59)	564(40)	564(39)	561(27)	529(58)
LDA	476(22)	538(21)	540(40)	584(58)	490(50)	515(75)	508(48)	512(69)
LASSO	498(25)	<b>472(40)</b>	<b>463(50)</b>	472(34)	506(42)	502(63)	488(42)	488(42)
SIR	<b>457(29)</b>	529(32)	486(54)	<b>441(31)</b>	479(43)	453(35)	<b>435(44)</b>	<b>456(42)</b>
CIR	515(32)	481(30)	476(37)	461(34)	<b>462(42)</b>	<b>443(46)</b>	469(34)	459(38)

Table 20: Prediction MSE/100 (standard deviation/100) of SVM for different DR methods and  $d$

DR \ d	1	2	3	4	5	6	7	8
raw	323(2)	322(2)	309(2)	307(1)	309(2)	305(2)	307(2)	307(1)
PCA	352(4)	350(6)	349(9)	349(10)	350(12)	344(5)	345(10)	332(8)
CPCA	353(4)	344(4)	351(11)	348(8)	347(9)	348(16)	346(7)	334(11)
LDA	352(2)	349(2)	350(2)	339(2)	333(2)	327(2)	326(2)	326(1)
LASSO	342(1)	333(2)	337(5)	321(5)	316(5)	311(3)	311(6)	312(5)
SIR	361(1)	362(1)	<b>304(1)</b>	308(1)	<b>309(2)</b>	306(2)	<b>306(2)</b>	<b>306(2)</b>
CIR	<b>323(2)</b>	<b>322(2)</b>	309(2)	<b>307(1)</b>	309(2)	<b>305(2)</b>	307(2)	307(1)

Table 21: Prediction MSE/100 (standard deviation/100) of GP regression for different DR methods and  $d$

DR \ d	1	2	3	4	5	6	7	8
raw	311(3)	341(12)	299(8)	298(10)	296(10)	292(6)	295(7)	291(7)
PCA	328(4)	323(2)	324(4)	324(2)	323(5)	323(3)	326(6)	325(4)
CPCA	330(5)	322(2)	324(3)	323(3)	322(2)	325(6)	324(3)	324(2)
LDA	337(3)	345(3)	341(6)	334(3)	338(5)	330(8)	327(7)	330(8)
LASSO	334(6)	<b>310(9)</b>	335(4)	336(11)	335(10)	329(4)	328(5)	330(3)
SIR	336(1)	342(4)	<b>285(6)</b>	299(11)	<b>295(6)</b>	296(7)	<b>293(7)</b>	<b>289(5)</b>
CIR	<b>311(3)</b>	341(12)	299(8)	<b>298(10)</b>	296(10)	<b>292(6)</b>	295(7)	291(7)

Table 22: Prediction MSE/100 (standard deviation/100) of neural network regression for different DR methods and  $d$

DR \ d	1	2	3	4	5	6	7	8
raw	319(5)	347(14)	516(*)	390(53)	410(53)	560(*)	595(*)	645(*)
PCA	*	*	*	*	*	*	*	*
CPCA	*	*	*	*	*	*	*	*
LDA	345(9)	349(13)	<b>378(16)</b>	392(21)	398(38)	<b>380(21)</b>	<b>399(29)</b>	<b>479(75)</b>
LASSO	344(32)	<b>324(9)</b>	*	*	*	*	*	*
SIR	343(5)	410(66)	605(*)	<b>379(36)</b>	<b>405(55)</b>	465(59)	513(*)	667(*)
CIR	<b>319(5)</b>	347(14)	516(*)	390(53)	410(53)	560(*)	595(*)	645(*)